International Journal of Climatology

International Journal of Climatology RMetS

RESEARCH ARTICLE

Projected Mid- and Late-Century Changes in Severe Convective Storms Across the United States From Dynamically Downscaled Climate Simulations

Caitlin M. Roufa[1] | Walker S. Ashley[1] | Alex M. Haberlie[1] | Jeremy M. Corner[1] | Kelvin T. Hawthorne[1] | Landon K. Moeller[1] | Vittorio A. Gensini[1] | Allison C. Michaelis[2]

[1]Department of Earth, Atmosphere, and Environment, Northern Illinois University, DeKalb, Illinois, USA | [2]Department of Marine, Earth, and Atmospheric Sciences, North Carolina State University, Raleigh, North Carolina, USA

Correspondence: Caitlin M. Roufa (croufa1@niu.edu)

Received: 31 March 2026 | **Revised:** 4 June 2026 | **Accepted:** 11 June 2026

ABSTRACT

Output from dynamically downscaled, convection-permitting regional climate simulations is used to examine projected changes in the frequency, timing and spatial distribution of synthetic severe convective storm (SCS) detections based on peril proxies across three 15-year epochs—1990–2005, 2040–2055 and 2085–2100—under intermediate and pessimistic emissions scenarios, including the first mid-century projections of SCS activity, providing a rare assessment of how SCS climatology may evolve throughout the 21st century. An explicit multi-hazard approach is employed to define severe convective perils using permutations of simulated upward vertical velocity and lowest model level reflectivity thresholds, allowing SCS activity to be assessed collectively for tornado, wind and hail perils. In response to enhanced greenhouse forcing and related changes in fundamental severe storm ingredients, projected synthetic SCS activity exhibits spatiotemporal changes relative to the historical baseline, including lengthening of the severe season, increases in the overall frequency of SCS days and an eastward shift of event frequency maxima. In addition to changes in mean frequency, results illustrate enhanced variability and increases in relatively high-activity days across all future epochs, driven by more frequent spring and early summer occurrences. Regionally, increases in SCS days are projected for south-central and Gulf Coast states, the southern Great Plains and the Midwest in the spring and the Midwest, Northeast and Southeast during the summer, while decreases are projected for the Great Plains during the summer. These changes are accompanied by a broadening geographic footprint of SCS activity, indicating a redistribution of severe storm risk under warming. Results provide physically grounded insight into the potential evolving severe storm landscape, which stakeholders, policymakers and the public may use to mitigate and build resilience against future events.

1 | Introduction

During the last three decades, severe convective storms (SCSs) in the contiguous United States (CONUS) have been responsible for nearly half a trillion USD in damage and thousands of fatalities (Black and Ashley 2010; A. B. Smith 2020; Gensini 2021; Strader et al. 2022; AON 2023), affecting all facets of the nation's economy, physical infrastructure and overall wellbeing. The frequency of SCS events and overall losses has increased significantly over the same period (Smith 2020; AON 2023), in part due to growing vulnerability and exposure resulting from population, agriculture and built-environment expansion (Ashley et al. 2014; Strader et al. 2017, 2024; Bundy et al. 2022). While increases in spatial vulnerability are an important factor in the changing SCS impact landscape, some uncertainty remains about how anthropogenic climate change (ACC) is influencing the climatology of SCS perils (tornado, severe hail and damaging wind; Gensini 2021) and, ultimately, how the SCS risk landscape may change in the future. A fundamental question asked by industry, policymakers, media and the broader public is, 'to what extent are potential future changes in the frequency, timing and spatial footprint of SCS attributable to ACC?'

Investigations into the effects of ACC on SCS activity have generally used two methods: an implicit or environmental proxy, approach (e.g., Trapp, Halvorson, et al. 2007; Van Klooster and Roebber 2009; Diffenbaugh et al. 2013; Robinson et al. 2013; Seeley and Romps 2015; Brimelow et al. 2017; Rasmussen et al. 2020; Glazer et al. 2021; Lepore et al. 2021; Wang et al. 2026) or an explicit approach (e.g., Sobash et al. 2008, 2011, 2016; Carley et al. 2011; Trapp et al. 2011; Clark et al. 2013; Robinson et al. 2013; Gensini and Mote 2014, 2015; Gallo et al. 2016; Hoogewind et al. 2017; Haberlie et al. 2022; Ashley et al. 2023; Kaminski et al. 2024; Rasmussen et al. 2023). Implicit studies, which often employ relatively coarse-resolution global climate model (GCM) output, examine changes in the fundamental ingredients required for SCS—moisture, instability (i.e., CAPE), convective inhibition (CIN) and shear. Implicit research has found that moisture, instability and CIN increase in some future CONUS climate scenarios, while projected subtle changes in shear may not be an important factor on days when SCSs are likely to occur (Brooks 2013; Tippett et al. 2015; Raupach et al. 2021; Gensini 2021). Broadly, findings examining the juxtaposition of these ingredients suggest that CONUS SCS frequency may increase in the future, but with marked regional variability (Hoogewind et al. 2017; Trapp et al. 2019; Lepore et al. 2021; Haberlie et al. 2022; Ashley et al. 2023; Gensini et al. 2024; Kaminski et al. 2024).

Explicit studies of SCS activity typically use an approach known as dynamical downscaling, a numerical modelling technique where relatively coarse-resolution GCM output or reanalysis data is used as the initial and lateral boundary conditions to force simulations, in this case using a convection-permitting regional climate model (CP-RCM), over long periods (e.g., 10- to 15-year epochs; Liu et al. 2017; Gensini et al. 2023; Rasmussen et al. 2023). These explicit simulations can effectively resolve thunderstorms, promoting the creation of a census of SCS events over simulation epochs that can, in turn, be used to assess changes in the projected climatology when epochs are compared. Studies have examined severe 'surrogates' or 'proxies' of perils (e.g., certain magnitudes of simulated radar reflectivity, updraft helicity [UH] and upward vertical velocity [UVV]) to create synthetic SCS climatologies (Robinson et al. 2013; Gensini and Mote 2014; Hoogewind et al. 2017). These proxy-derived or 'synthetic' SCS climatologies suggest that SCSs may increase in frequency and variability by the end of the century (Trapp et al. 2011, 2019; Gensini and Mote 2015; Trapp and Hoogewind 2016; Hoogewind et al. 2017; Rasmussen et al. 2020; Prein 2023).

In this study, we extend existing explicit convection-permitting projections of SCS by employing the dynamically downscaled output described by Gensini et al. (2023), introducing the first mid-century projections of SCS activity for multiple climate pathways in addition to end-of-century assessments. The simulation output spans three 15-year epochs, including a historical baseline, as well as mid- and end-of-21st-century periods under two future greenhouse gas emission pathways representing intermediate and pessimistic emissions, yielding 75 years of high-resolution simulation output. From these simulations, we generate synthetic SCS peril detections across multiple hazard types (tornado, wind and hail), rather than in isolation and explicitly quantify changes in both the frequency and statistical distribution tail behaviour of daily event activity. Beyond frequency changes, we diagnose spatial reorientation of SCS activity using centroid shifts, dispersion ellipses and changes in areal extent, providing a quantitative framework for assessing how the geographic footprint of SCS evolves under warming. Together, these results provide a physically grounded, high-resolution perspective of how SCS perils may evolve throughout the 21st century, with direct implications for risk assessment, preparedness and resilience in the face of rapid environmental and societal change.

2 | Methods

2.1 | Regional Climate Model Output

SCS proxies were produced using output from CP-RCM simulations generated using the Advanced Research Core of the Weather Research and Forecasting Model version 4.1.2 (WRF-ARW; Skamarock et al. 2019). Model configuration is considered convection-permitting, with a horizontal grid spacing of 3.75 km, spanning 51 vertical levels over the CONUS and adjacent parts of Canada and Mexico. NCAR's bias-corrected Community Earth System Model (CESM) served as initial and lateral boundary conditions for the Gensini et al. (2023) simulations known as WRF-Bias Corrected CESM (WRF-BCC). Bias correction employed the use of the 1981–2005 ERA-Interim reanalysis (Dee et al. 2011) following the methods in Bruyère et al. (2014). WRF-BCC historical simulations (HIST) were compared to historical reanalyses of spatial patterns of temperature and precipitation, with only minor regional and seasonal biases. These included: a warm-season dry bias in the Southeast; a cool-season cold bias east of the Rocky Mountains; and a warm-season dry bias in the Great Plains that was notably reduced compared to other RCMs (Liu et al. 2017; Haberlie and Ashley 2019; Gensini et al. 2023). Additional WRF-BCC verification details are available in Gensini et al. (2023).

The three 15-hydrologic-year (1 October–30 September) epochs include a historical period from 1990 to 2005 (HIST), a mid-21st-century period from 2040 to 2055 (MID) and an end-of-21st-century period from 2085 to 2100 (END). ACC trajectories were produced for both the MID and END epochs following the representative concentration pathways (RCPs) for intermediate (RCP4.5) and pessimistic (RCP8.5) greenhouse gas emissions scenarios (Moss et al. 2010; IPCC 2014). The Gensini et al. (2023) workflow is not a pseudo-global warming (PGW) approach (e.g., Trapp and Hoogewind 2016; Liu et al. 2017) since the simulations incorporate both projected thermodynamic and kinematic changes from the GCM. This is advantageous as the simulations account for changes in the general circulation and modes of climate variability that alter environments and fundamental ingredients supportive of SCSs.

2.2 | Storm Report Data

Synthetic SCS generated from the HIST output are compared with storm reports from the Storm Prediction Center (SPC)

Severe Weather Database for the 1990–2005 period (SPC 2024) to assess and calibrate the spatiotemporal frequency of synthetic perils from HIST over a 15-year period. Reports of all tornadoes, large hail ≥ 1.9 cm considered severe by the NWS before 2010 (and ≥ 2.54 cm thereafter) and non-tornadic severe wind ($\geq 26\,\mathrm{m\,s^{-1}}$) are mapped to an 80-km grid, which corresponds to the SPC verification method that assesses reports within 40 km (25 miles) of a point. Documented limitations with this database include observation biases related to population density (Trapp et al. 2006; Allen and Tippett 2015) as well as damaging wind reports generated from observations of agricultural, built- and natural-environment damage rather than direct measurements of speeds (Weiss 2002; Trapp et al. 2006; Edwards et al. 2018; Tirone et al. 2024) and advances in remote sensing and other technologies (P. L. Smith 1999). In addition, evolving NWS severe hail reporting practices introduce observational inhomogeneities; however, proxy calibration is internally consistent, as it is performed prior to changing hail criteria. Despite these limitations, the SPC Severe Weather Database is the best available dataset of observations to compare against HIST.

2.3 | Synthetic SCS Peril Proxies

Since SCS perils cannot be explicitly simulated in the model, an SCS proxy is used. Herein, a proxy is defined as a model-derived diagnostic variable or combination of variables above a threshold that serves as a surrogate for SCS perils. The performance of SCS proxies was evaluated for skill by comparing the HIST output with SPC storm reports, permitting identification of threshold ranges for selected model variables that maximise correspondence between simulated synthetic peril counts and SPC reports. This process provides a meaningful basis for projecting SCS changes in future epochs.

To assess which SCS proxy most effectively represents observed perils, hourly maxima of three variables from the WRF-BCC output—UH, UVV and downward vertical velocity (DVV)—were examined in combination with simulated instantaneous lowest model level radar reflectivity factor (Z), which was used to determine the presence of convective precipitation (≥ 40 dBZ). These variables have been employed in prior studies that examined changes in SCS proxies (Table 1). Following Gensini and Mote (2014, 2015), synthetic SCS proxies are created by combining threshold exceedance masks of UH, UVV or DVV with thresholded Z exceedance masks so that only coincident threshold exceedances are retained. While UH incorporates vertical wind and rotation, UVV and DVV capture vertical motion that may occur independently of strong rotation, thereby enhancing sensitivity to the full spectrum of SCS perils and storm modes.

Simulated UH estimates the strength of rotating updrafts (i.e., associated with mesocyclones and other rotating convection) and is frequently used as a severe proxy for forecasting tornadic supercells and examining future trends in SCSs (Sobash et al. 2008, 2011, 2016; Carley et al. 2011; Trapp et al. 2011; Clark et al. 2013; Gensini and Mote 2015; Hoogewind et al. 2017; Ashley et al. 2023). WRF-BCC output includes hourly maximum, mid-level (2–5 km) UH ($\mathrm{m^2\,s^{-2}}$), calculated as the vertical integral of the product of vertical velocity and the vertical component of relative vorticity (Kain et al. 2008). This research considers only positive (i.e., cyclonic) UH. UVV ($\mathrm{m\,s^{-1}}$), provided as the hourly maximum positive vertical velocity from the first model level through 400 hPa, describes the intensity of upward convection. UVV is related to CAPE via parcel theory, where the theoretical maximum $w = \sqrt{2\,\mathrm{CAPE}}$. Although UH incorporates a vertical wind component, UVV accounts for strongly buoyant but not necessarily rotating updrafts that may still produce severe hail and damaging winds.

Simulated DVV ($\mathrm{m\,s^{-1}}$) is the hourly maximum negative vertical velocity from the lowest model level through 400 hPa and describes the intensity of downward motion in a storm that may indicate potential for severe hail and non-tornadic, severe winds (Sobash et al. 2008). Including DVV as a proxy permits the detection of events characterised by intense downdrafts, such as downbursts or microbursts, which may not be associated with strong rotation or updrafts.

2.4 | Verification and Calibration of Proxy Thresholds

Minimum threshold values for UH, UVV, DVV and Z were calibrated through comparison of HIST proxy detections with SPC storm reports aggregated to the 80-km grid. SPC reports were assigned to the nearest coarsened WRF-BCC grid point using nearest-neighbour assignment based on the report's latitude and longitude. The WRF-BCC proxy fields were first aggregated from the native 3.75-km grid to the 80-km grid using 20×20 grid cell blocks, and report counts were accumulated at the nearest coarsened grid point for each 1200–1200 UTC analysis day. Verification of SCS proxies against observed perils is necessary given the wide range of minimum threshold values reported in the literature (Table 1) for UH (Sobash et al. 2008, 2011, 2016; Carley et al. 2011; Trapp et al. 2011; Clark et al. 2013; Gensini and Mote 2015; Gallo et al. 2016; Hoogewind et al. 2017), in addition to limited research employing UVV (Sobash et al. 2008; Hoogewind et al. 2017) and DVV (Sobash et al. 2008). Proxy behaviour is also sensitive to model configuration (e.g., grid spacing, microphysics and boundary conditions) and may exhibit regional or seasonal biases (Hoogewind et al. 2017; Sobash and Kain 2017). These factors necessitate independent calibration and verification for detecting synthetic perils prior to application in future climate epochs.

Verification herein follows Sobash et al. (2011), where simulation output is first converted to binary daily event fields and subsequently evaluated using spatial, temporal and frequency verification approaches. For each proxy threshold combination, daily WRF-BCC output is evaluated over 1200–1200 UTC convective days and assigned a value of 1 at grid cells exceeding the specified threshold and 0 otherwise on the native model grid. These daily binary proxy fields are then coarsened to the 80-km grid to match the spatial aggregation of SPC report-day observations. SPC reports are similarly converted to daily binary fields, where a grid cell is assigned a value of 1 if at least one report occurred within that grid cell during the convective day and 0 otherwise. Following binary conversion and spatial aggregation, daily proxy and SPC fields are concatenated along the time dimension, then summed to produce climatological count fields that represent the number of SCS days at each grid point.

TABLE 1 | Summary of severe proxy threshold values for UH, DVV, UVV and *Z* from the literature.

UH ($m^2 s^{-2}$)

Study	Threshold	*Z* (dBZ)	WRF grid spacing (km)	Vertical levels	Microphysics scheme
Sobash et al. (2008)	54	54.875	4.0	35	WSM6
Carley et al. (2011)	Weak: 30	40	4.25	—	Purdue Lin
	Moderate: 50	40			
	Strong: 70	40			
Trapp et al. (2011)	40	50	4.25	35	WSM6
Sobash et al. (2011)	41	—	4.0	35	WSM6
Clark et al. (2013)	100	—	4.0	—	Multiple–Ensemble
Gensini and Mote (2014)	60	40	4.0	35	WSM6
Gensini and Mote (2015)	60	40	4.0	35	WSM6
Gallo et al. (2016)	75	—	4.0	—	WSM6
Sobash et al. (2016)	75	—	3.0	—	Multiple–Ensemble
Hoogewind et al. (2017)	35	—	4.0	45	Thompson

DVV ($m\ s^{-1}$)

Study	Threshold	*Z* (dBZ)	WRF grid (km)	Vertical levels	Microphysics scheme
Sobash et al. (2008)	−6	54.875	4.0	35	WSM6

UVV ($m\ s^{-1}$)

Study	Threshold	*Z* (dBZ)	WRF grid (km)	Vertical levels	Microphysics scheme
Sobash et al. (2008)	23.25	54.875	4.0	35	WSM6
Hoogewind et al. (2017)	22	—	4.0	45	Thompson

***Z* (dBZ)**

Study	Threshold	*Z* (dBZ)	WRF grid (km)	Vertical levels	Microphysics scheme
Haberlie et al. (2022)	Weak: 40	—	3.75	51	Thompson
	Strong: 50–60				
Robinson et al. (2013)	45, 50 and ave. 45 + 50	—	4.25	35	WSM6

Proxy thresholds were evaluated using a set of complementary diagnostics designed to jointly constrain event frequency, temporal agreement and spatial realism. First, the domain mean bias ratio is calculated between SCS proxy days and SPC report days to enforce realistic climatological frequency. Second, temporal agreement is assessed using the root mean square error (RMSE) of standardised annual domain mean sum of grid point days, which emphasises coherence in interannual variability while reducing sensitivity to differences in mean event frequency between SCS proxy days and SPC report days. This approach follows prior proxy evaluation frameworks that combine frequency constraints with error-based measures of time-varying agreement (Hoogewind et al. 2017). Third, spatial realism is quantified using a neighbourhood-based spatial pattern correlation between the SCS proxy and climatological mean SPC report day maps. A radius-1 neighbourhood operator corresponding to a 3×3 grid cell moving window, allowing spatial displacement up to ~240 km, is applied to account for expected spatial displacement between SCS proxy footprints and point-based SPC reports and to mitigate the 'double penalty problem' inherent to grid point verification of high-resolution fields (Ebert 2008, 2009; Gilleland et al. 2009; Gilleland et al. 2010). Neighbourhood smoothing in this context defines an acceptable regional tolerance for climatological comparison, rather than serving as a standalone optimisation metric.

While this neighbourhood spatial method addresses broad spatial correlation, a second spatial method called fraction skill score (FSS; Roberts and Lean 2008), a neighbourhood-based spatial verification approach, is used to compare the fractional coverage or overlap of events within a moving neighbourhood window. Climatological synthetic SCS exceedance fields are provided as inputs to the PySteps FSS function (Pulkkinen et al. 2019), along with a specified threshold value used by the function to generate binary exceedance maps (e.g., grid cells exceeding a specific number of SCS days). Then fractional coverage is computed within a moving window of fixed size, and the

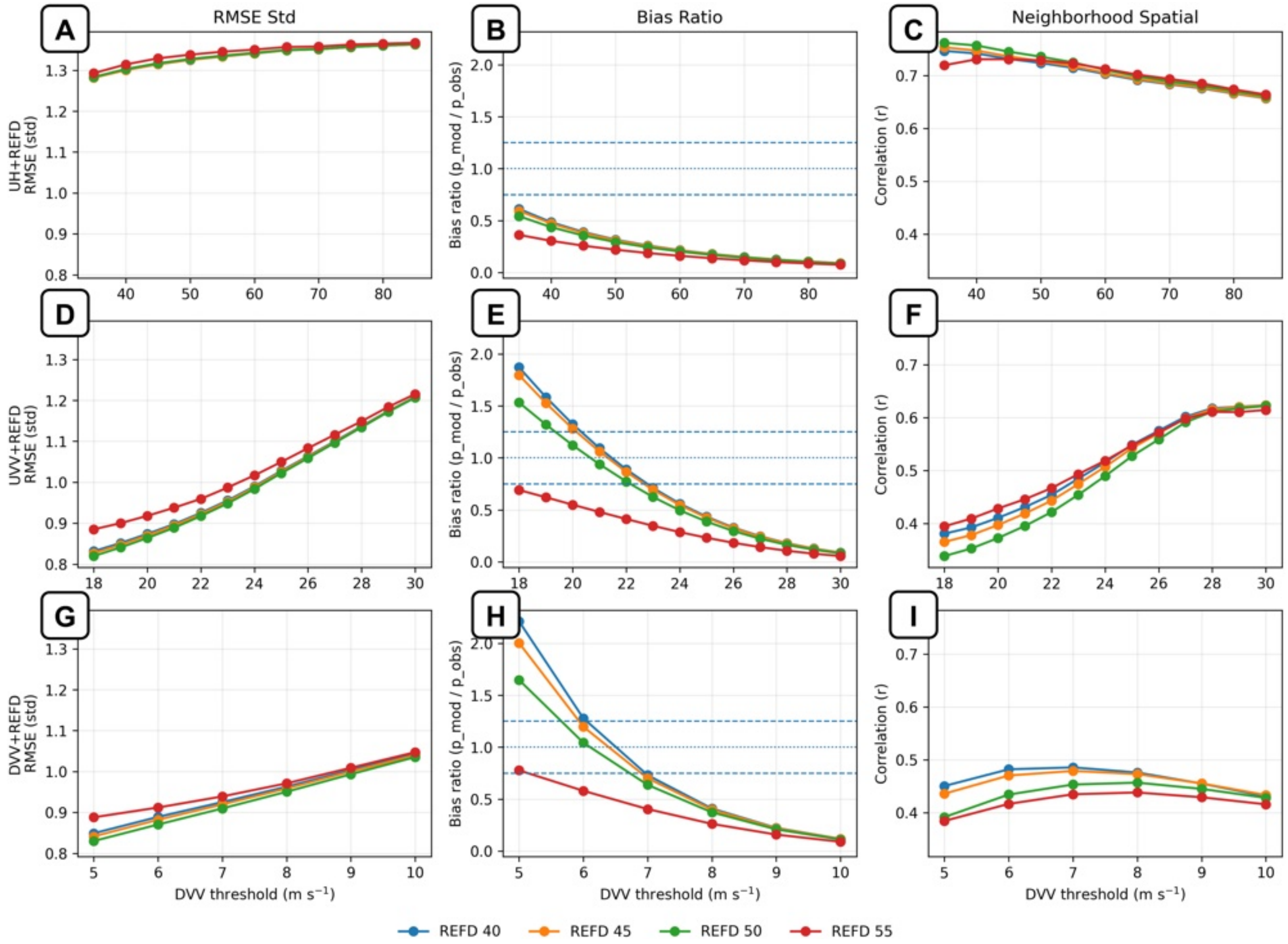

FIGURE 1 | Sensitivity of proxy verification metrics to primary threshold choice for UH + *Z* (A–C), UVV + *Z* (D–F) and DVV + *Z* (G–I). Columns show RMSE of standardised annual domain mean SCS days, bias ratio between SCS proxy days and SPC severe days and neighbourhood spatial pattern correlation ($r = 1$; 200-km tolerance). Coloured lines denote *Z* thresholds. Dashed horizontal lines in the bias panels indicate ±25% departures from frequency match. [Colour figure can be viewed at wileyonlinelibrary.com]

mean squared difference between proxy and observed fractions is compared (Roberts and Lean 2008; Ebert 2009).

The sensitivity of each verification metric to primary threshold choice is illustrated in response curves for UH + *Z* (Figure 1A–C), UVV + *Z* (Figure 1D–F) and DVV + *Z* (Figure 1G–I). For each proxy family, panels show the dependence of standardised RMSE (Figure 1A,D,G), bias ratio (Figure 1B,E,H) and neighbourhood spatial correlation (Figure 1C,F,I), with coloured lines denoting different *Z* thresholds. These response curves demonstrate systematic trade-offs between frequency realism, temporal agreement and spatial correspondence as thresholds are varied and provide a transparent basis for proxy selection without reliance on a single scalar score or metric. Each proxy family is evaluated in HIST against individual SPC peril reports (tornado, wind and hail) and all perils combined using FSS across the tested threshold space (Figure 2). For UH + Z, the range of highest spatial agreement for wind and hail detections exhibits close overlap between approximately 35–60 m^2 s^{-2} in conjunction with 40–55 dBZ (Figure 2F–H), while tornado detections favour higher UH thresholds between approximately 65–85 m^2 s^{-2} with 40–50 dBZ (Figure 2E). This behaviour represents the dynamical structure of tornadic storms, which are often characterised by stronger rotational signatures relative to precipitation intensity compared to other perils (Sobash et al. 2008; Trapp et al. 2011; Clark et al. 2013; Gensini and Mote 2014, 2015). The spatial skill for UH + *Z* for all perils lies within the same range as for wind and hail.

For UVV + *Z*, wind, hail and combined-perils detections exhibit overlapping ranges of skilful spatial agreement between approximately 18–27 m s^{-1} in conjunction with 40–50 dBZ (Figure 2B–D), while tornado detections favour somewhat higher and more discrete UVV thresholds within this range (Figure 2A). Like UH and UVV, DVV exhibits overlap for wind and hail in the most skilful ranges between approximately 5–8 m s^{-1} and 40–50 dBZ (Figure 2J–K), with comparatively narrower skilful ranges for tornado detections between approximately 8–9 m s^{-1} and 40–50 dBZ (Figure 2I).

Because FSS is sensitive to event frequency bias, displacement and neighbourhood scale (Skok 2015; Skok and Roberts 2016, 2018; Wilks 2019; Mittermaier 2021; Antonio and Aitchison 2025), spatial agreement is interpreted in conjunction with bias ratio and standardised RMSE diagnostics

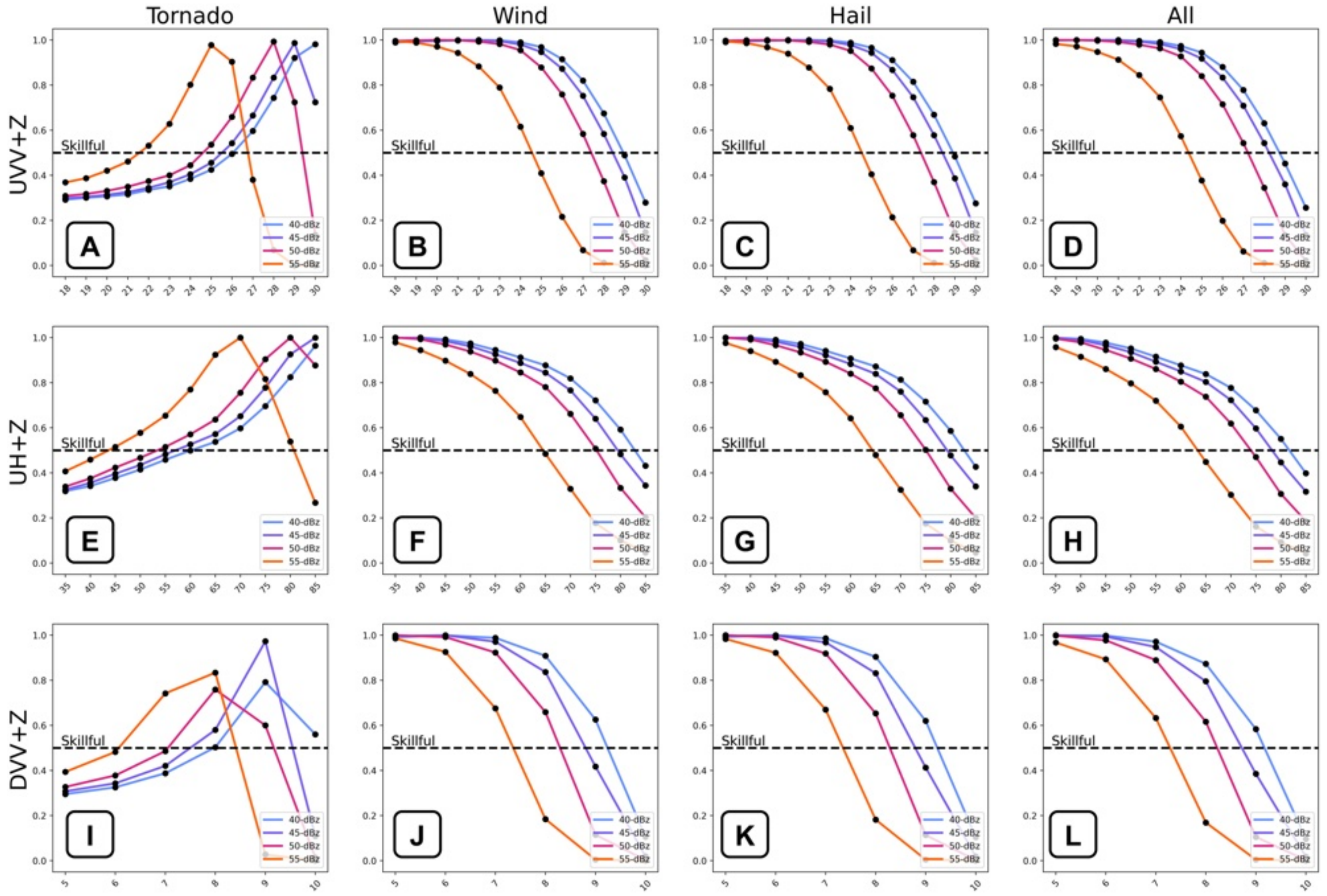

FIGURE 2 | Fraction skill score (FSS) for tornado, wind, hail and all perils combined, shown for UVV + Z (A–D), UH + Z (E–H) and DVV + Z (I–L) proxies. Scores are plotted as a function of synthetic proxy thresholds (x-axis) with reflectivity (Z) indicated by colour and skill (y-axis). FSS values were calculated for each proxy, with the dashed line marking the 0.5 threshold, above which forecasts are considered skilful. [Colour figure can be viewed at wileyonlinelibrary.com]

rather than in isolation. FSS values approaching unity at lower thresholds represent broad spatial overlap between proxy footprints and observed event regions, so proxy candidates are then filtered using frequency and temporal constraints. Given these limitations and that this FSS-based assessment confirms that multiple threshold combinations within each proxy family achieve spatially skilful agreement, final proxy selection is not based solely on FSS magnitude but rather on the combined behaviour of frequency realism, temporal agreement and spatial correspondence within the spatially skilful threshold window.

Comparison across proxy families reveals distinct calibration behaviour. UH-based proxies exhibit high neighbourhood spatial correlations across the evaluated threshold space (Figure 1C) but underproduce SCS days relative to observations (Figure 1B), with frequency and bias worsening as thresholds increase. DVV-based proxies can achieve bias ratios closer to unity over a limited threshold range (Figure 1H) but exhibit weaker spatial correspondence (Figure 1I) and reduced detection frequency for combined perils. In contrast, UVV-based proxies display a clear bias-neutral threshold window within a broader range of spatially skilful thresholds (Figure 1E) in addition to lower standardised RMSE (Figure 1D) and moderate neighbourhood spatial correlation (Figure 1F). Within the UVV family, thresholds between approximately 18–27 m s^{-1} paired with 40–50 dBZ satisfy spatial skill constraints while retaining acceptable frequency behaviour.

Finally, threshold selection is guided by annual climatological frequency realism while maintaining strong temporal and spatial agreement. Based on these joint constraints, a threshold of 21 m s^{-1} for UVV combined with $Z \geq 40$ dBZ provides near-unity annual bias, low standardised RMSE, moderate neighbourhood spatial correlation and skilful FSS performance across perils. The proxy is broadly representative of activity in the Great Plains through the Midwest, though it underestimates annual activity in the northeast (Figure S1). Although stricter thresholds reduce bias on a seasonal basis, they systematically suppress peak-season detections and under-represent the observed annual SCS climatology. The selected threshold, therefore, provides the most balanced representation of annual SCS frequency and spatial structure; however, it should not be interpreted as a direct classifier of specific hazard types or their realised intensities. The calibrated SCS proxy threshold is applied uniformly across the domain to HIST, MID and END epochs to generate synthetic SCS climatologies used in the results. This approach ensures that projected changes represent differences in the simulated convective environment rather than differences in proxy definition across climate states.

TABLE 2 | Central tendencies (annual climatological means, medians, standard deviation and relative change); significance testing (p values computed using the Mann–Whitney U-test) and coefficient of variation (CV) of synthetic severe convective storm (SCS) counts and days between each future epoch and the historical period (HIST).

Synthetic SCS counts	HIST	MID4.5	MID8.5	END4.5	END8.5
Mean	31,920	40,298	41,189	43,841	56,659
Relative change vs. HIST (%)	—	26.2	29.0	37.3	77.5
Median	33,401	40,009	43,574	46,649	60,247
Relative change vs. HIST (%)	—	19.8	30.5	39.7	80.4
Standard deviation	10,686	13,935	13,884	15,501	16,494
CV (%)	33.5	34.6	33.7	35.4	29.1
p	—	0.0167	0.0109	0.0056	0.00003
Synthetic SCS days	**HIST**	**MID4.5**	**MID8.5**	**END4.5**	**END8.5**
Mean	5417	6513	6708	6984	8421
Relative change vs. HIST (%)	—	20.2	23.8	28.9	55.5
Median	5731	6563	7130	7321	9102
Relative change vs. HIST (%)	—	14.5	24.4	27.8	58.8
Standard deviation	1646	1915	1909	2038	2311
CV (%)	30.4	29.4	28.5	29.2	27.4
p	—	0.0167	0.0109	0.0056	0.00003

Note: p values <0.05 indicate significant changes with respect to HIST.

2.5 | Spatial Analysis of SCS Climatologies

For each epoch (HIST, MID4.5, MID8.5, END4.5 and END8.5), the previously assessed and optimised synthetic proxy UVV + Z threshold is used to create fields of synthetic SCS proxy detections, which are summed at each 80-km grid point over the 15-year period to create spatial climatologies for the eastern CONUS (ECONUS, east of the Rocky Mountains) domain. Deltas or differences in both total and annual mean synthetic SCS counts between future and historical epochs that illustrate projected changes to SCS frequency are calculated by taking the difference at each grid cell between each of the future epochs relative to the HIST epoch. Throughout this manuscript, 'SCS counts' refers to the total number of synthetic SCS proxy exceedances and 'SCS days' refers to binary grid cell daily occurrence (one or more detections within a 1200–1200 UTC day).

To characterise projected changes in the spatial centre, distribution and dispersion extent of SCS activity, weighted centroids and standard deviational ellipses were computed from annual and seasonal mean SCS days for each epoch, masked where there were <1 day/year per grid point. Centroids were calculated from grid cell coordinates weighted by mean SCS days per year and latitude. Standard deviation ellipses were derived from the eigendecomposition of the weighted spatial covariance matrix following Lefever (1926) and Wang et al. (2015). Ellipse orientation, major and minor axis lengths and ellipse area were used to characterise the orientation, spatial dispersion and areal extent of climatological SCS distributions, as in prior work characterising seasonal tornado activity (Moore and McGuire 2019).

3 | Results

3.1 | Temporal Trends in SCS Activity

Projected synthetic SCS counts and days both significantly increase across all future epochs (Table 2), consistent with a growing body of literature supporting similar trends in modelled SCS and convective hazard frequencies for historical through the end of the 21st century under ACC (Del Genio et al. 2007; Trapp, Diffenbaugh, et al. 2007; Trapp et al. 2009; Van Klooster and Roebber 2009; Robinson et al. 2013; Gensini and Mote 2014, 2015; Hoogewind et al. 2017; Glazer et al. 2021; Haberlie et al. 2022; Ashley et al. 2023; Kaminski et al. 2024). The smallest increases in SCS counts occur in MID4.5, while END8.5 has the most dramatic rise in SCS counts. Ashley et al. (2023) also found potential increases in supercell counts (up to 27%) by the end of the 21st century, while Hoogewind et al. (2017) projected a dramatic increase in SCS counts (up to 150%) by the end of the 21st century when using UVV as an SCS proxy, reinforcing the broader consensus on increased SCS potential in a warming climate. Our results fall in this range and provide additional clarity on the possible changes in the spatiotemporal magnitudes during the 21st century, including a unique set of midcentury perspectives.

In addition to an increase in the frequency of synthetic SCS counts and days, interannual variability (as measured by standard deviation of annual totals) in SCS counts and days is projected to increase by the middle and end of the 21st century compared with the historical baseline, similar to what Gensini and Mote (2015) found for the spring in their simulations. However, the coefficient of variation (CV) remains nearly constant across epochs

(27%–35%; Table 2), indicating that interannual variability scales proportionally with the mean. Therefore, there is a projected shift in central tendency rather than a statistically robust change in interannual variability. Although MID4.5, MID8.5 and END4.5 epochs all show increases in both SCS counts and days over HIST, their annual totals remain comparable to one another (Figure 3). In contrast, the END8.5 scenario stands out with markedly higher SCS event counts and days than all the other epochs, suggesting greater sensitivity to the higher emissions pathway by the end of the 21st century.

3.2 | Seasonal Shifts

Simulations project a consistent trend towards earlier seasonal onset of SCSs by the middle and end of the 21st century in all ACC trajectories, with SCS frequency escalating as early as February and March across much of the ECONUS (Figures 3 and 4). This echoes prior research by Lee (2012), who found increasing frequency of strong tornado days in the early spring under multiple GCMs and emissions scenarios; Ashley et al. (2023), who projected an increase in supercell frequency in late winter and early spring; and Hoogewind et al. (2017), who found a statistically significant lengthening of the SCS season. Spring (MAM) has particularly strong increases in both mean counts and variability across all scenarios, with June consistently the seasonal peak across epochs (Figure 4). August is notable in that there are no large changes in SCS variability and counts. END8.5 diverges from the other epochs with substantial projected increases in SCS frequency from April through July and a secondary increase in October through December. Our finding of projected increased springtime SCS frequency and decreased summer SCS frequency in some regions, including parts of the Great Plains (Figure S2), aligns with end-of-21st-century seasonal patterns of supercells reported in Ashley et al. (2023).

SCS frequency is projected to intensify with consistent increases across all epochs for October, while END8.5 shows particularly large gains in February and elevated variability for all END epochs during the winter months. December has a modest but consistent rise in mean SCS counts for all epochs.

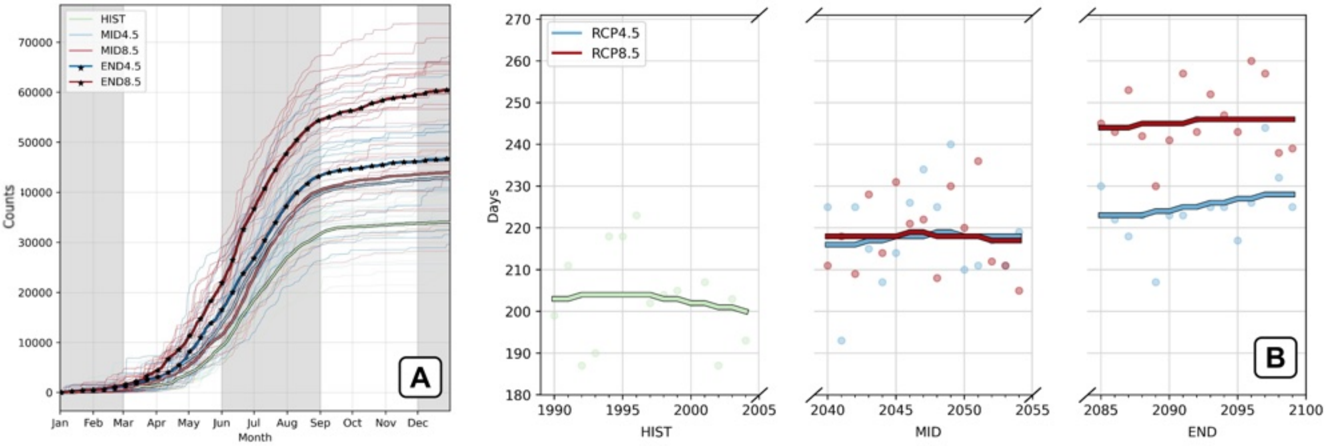

FIGURE 3 | (A) Cumulative frequency diagram of synthetic SCS peril counts for each epoch, with annual means plotted in bold. HIST is shown in green, RCP4.5 in blue and RCP8.5 in red, with asterisks marking the END epoch. (B) Time series of SCS days for each epoch, smoothed via a 5-year Gaussian mean, with annual means for each year shown as scatter points. Colours as in (A). [Colour figure can be viewed at wileyonlinelibrary.com]

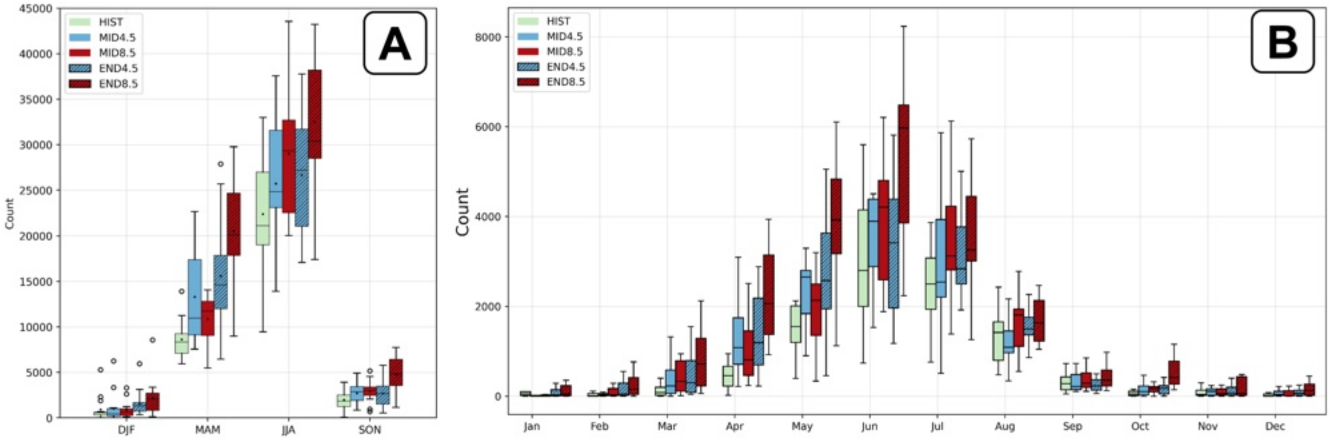

FIGURE 4 | (A) Seasonal counts of synthetic SCS activity for each epoch, shown as bar charts with HIST in green, RCP4.5 in blue, RCP8.5 in red and hatching indicating END. Dots indicate (B) Monthly counts of synthetic SCS for each epoch, with colours as in (A). [Colour figure can be viewed at wileyonlinelibrary.com]

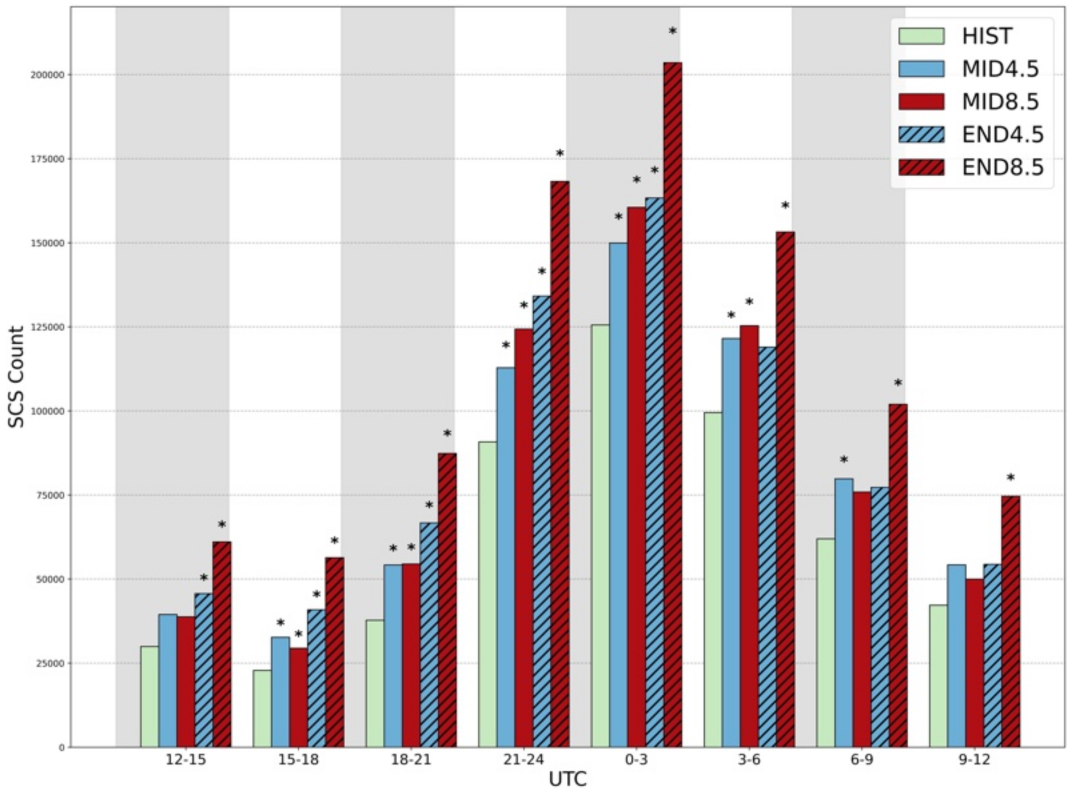

FIGURE 5 | Diurnal distribution of synthetic SCS count for each epoch. Raw SCS counts are binned by 3-h intervals for readability. RCP4.5 is shown in blue and RCP8.5 in red, with hatching denoting the end-of-century epoch, and no hatching indicates the middle-of-century epoch. Green indicates HIST. Asterisks indicate statistical significance ($p \leq 0.05$) based on the Mann–Whitney U-test. [Colour figure can be viewed at wileyonlinelibrary.com]

3.3 | Diurnal Cycle

Across all future epochs, synthetic SCS counts increase throughout the diurnal cycle, with the most pronounced changes occurring during the late afternoon and evening hours (2100–1000 UTC), especially for END8.5 (Figure 5). While the timing of daily peaks in and distribution of peril counts remains similar to HIST during the diurnal cycle for all epochs, the magnitude of SCS counts grows, especially under END8.5. An increase in the number of projected SCS events during evening hours may have implications for vulnerability, as these events coincide with periods of reduced public awareness, shelter access and forecast skill (Bunker et al. 2019; Brown et al. 2021), which could result in increases in SCS-related (e.g., nocturnal tornado) fatalities (Ashley et al. 2008; Strader et al. 2022).

3.4 | Spatial Trends in SCS Activity

By the middle and end of the 21st century, simulations project a considerable spatial shift of synthetic SCS activity with distinct seasonal variation (Figures 6 and 7, Figure S2). Winter (DJF) mean SCS frequency remains cantered along the Gulf Coast for both the middle and end of the 21st century and all ACC trajectories; however, future projections show a significant increase in mean annual SCS days in locations around the Gulf and in the Deep South, with up to an additional two SCS days representing relative increases of well over 100% (Figure S2).

In spring (MAM), SCS frequency is concentrated in the southern and central Great Plains with a marked expansion into the Midwest and Deep South for all epochs. Locations in the Deep South, with the addition of those in the southern Great Plains, are projected to see significant increases of up to six SCS days in the spring season, corresponding to greater than 100% gains and indicating a broader spatial footprint—and therefore, potential for larger socioeconomic exposure (Strader et al. 2024)—for spring SCS events.

Most summer (JJA) SCS days are projected to continue to occur in the northern and central Great Plains and parts of the Southeast (Figure 8); however, projections suggest declines of up to four SCS days in the central Great Plains, which is a ~50% reduction relative to HIST. Meanwhile, the Midwest, Northeast and Southeast are projected to have statistically significant increases of 1 to more than 6 days, which is over a 100% increase above HIST. These results suggest a weakening of historical summer SCS frequency corridors in the Great Plains and an eastward shift of the broader SCS climatology towards more densely populated areas in the future.

In the fall (SON), SCS frequency is projected to remain focused in the Great Plains and Midwest. Increases of up to two SCS days are expected to occur in locations in a corridor from the

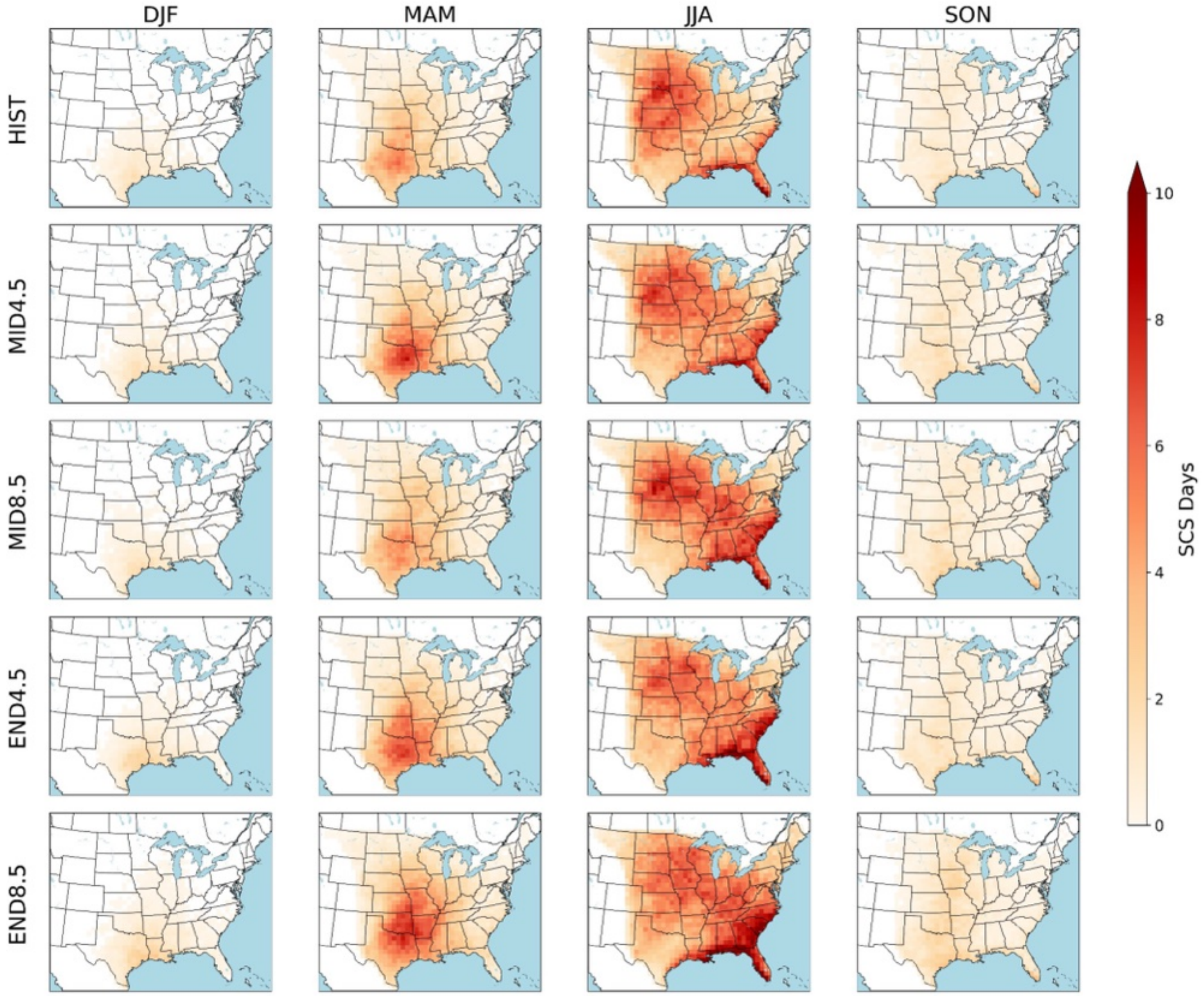

FIGURE 6 | Spatial climatology on an 80-km grid of synthetic mean annual SCS days for each epoch (rows) and season (columns). An SCS day is defined as a day with one or more perils occurring within the 80-km grid cell. White shading indicates no change or areas outside the domain, while orange and red shading indicate higher SCS day counts. [Colour figure can be viewed at wileyonlinelibrary.com]

southern Great Plains through the Midwest, with relative increases in SCS days of over 100%, reflecting an extension of the SCS season into the late transition season.

Spatial centre, distribution and areal extent of mean SCS days are quantified using centroid analysis for the annual and seasonal means of each epoch (Figure 9). The annual mean centroid shifts from the central Great Plains towards the Southeast in all future epochs from HIST by 121–227 km (Figure 9A, Table 3). DJF centroids remain located along the Gulf Coast, with an eastward shift of 127–227 km (Figure 9B, Table 3). In MAM, centroids are centred in the southern Great Plains with a vector shift to the east-northeast by 114–250 km (Figure 9C, Table 3). JJA centroids are similar to the annual distributions but show a larger projected spatial shift of 150–321 km towards the east-southeast (Figure 9D, Table 3). Except for END8.5, which has a northwestward trajectory from the historical baseline, SON centroids, exclusively fixed over the Deep South, shift southwestward by 186–253 km (Figure 9E, Table 3). These centroid locations and shifts are consistent with spatial climatologies and corresponding deltas for each epoch (Figures 6–8) and with observed historical tornado centroid location and migration described by Moore and McGuire (2019). While centroid locations describe the spatial centre of SCS activity, dispersion ellipses characterise the spread and orientation of the distribution.

Standard deviational ellipses quantify the projected mean annual and seasonal spatial distributions for each epoch, giving an indication of the core spatial distribution and areal extent of SCS days (Figure 9, Table 3). The greatest changes in distribution are observed in DJF, with areal extent projected to increase by 39%–161% by mid- and end-of-century. MAM distribution is centred over the southern Great Plains and Deep South, extending northward through the Midwest, with projected area changes of 6.5%–57%. Of note is the greater area change and ellipse elongation towards the Midwest in the RCP8.5 emissions scenarios. Distribution is along an axis extending from the northern Great Plains through the Southeast, corresponding to

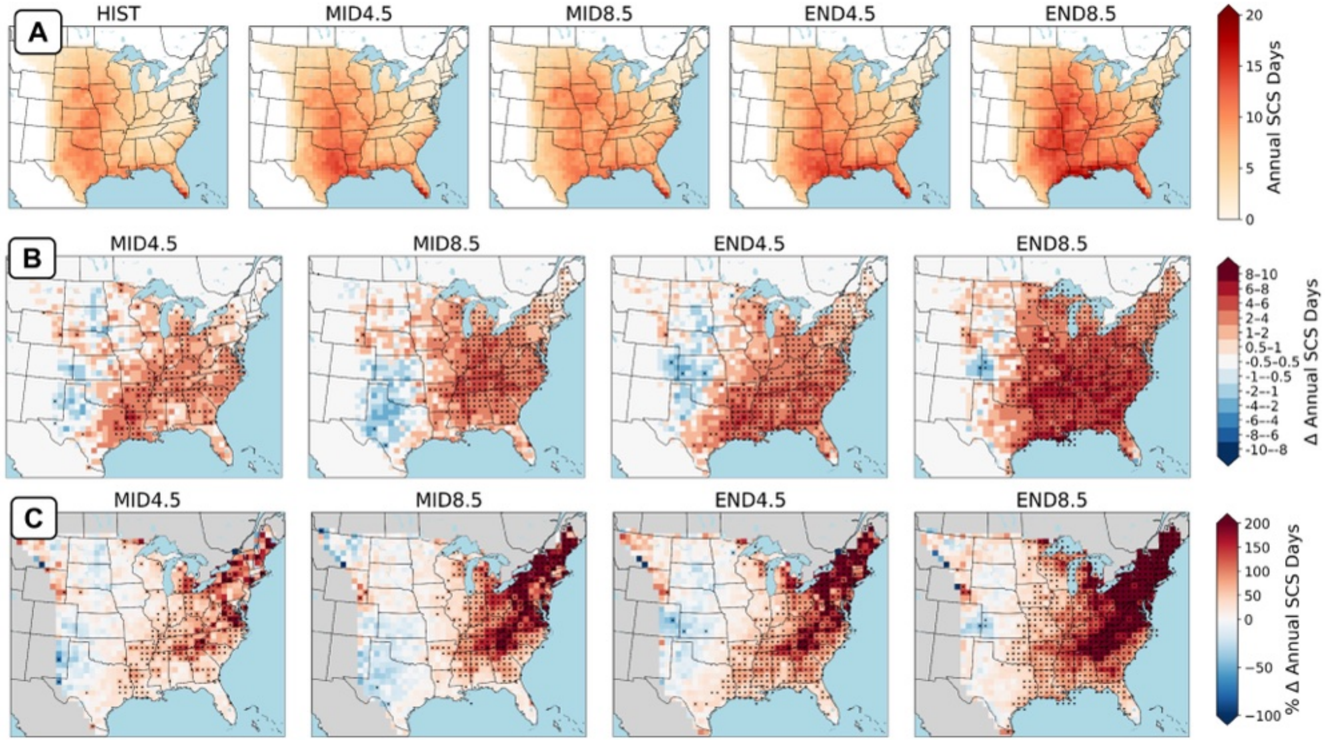

FIGURE 7 | (A) Spatial climatology on an 80-km grid of synthetic annual mean SCS days for each epoch. An SCS day is defined as a day with one or more perils occurring within the 80-km grid cell. White shading indicates no change or areas outside the domain, while orange and red shading indicate higher SCS day counts. (B) Spatial deltas showing the difference between each epoch and HIST in annual mean SCS days, with red shading indicating increases and blue shading indicating decreases. (C) Per cent change in annual mean SCS days between each epoch and HIST, with red shading indicating increases and blue shading indicating decreases. Stippling marks regions of statistical significance based on the Mann–Whitney *U*-test. [Colour figure can be viewed at wileyonlinelibrary.com]

the climatological distribution of SCS days (Figure 6). JJA area changes are smaller than those in winter, with a 7%–19% increase in distribution extent. SON exhibits more variability in distribution and area than other seasons, centred in the Deep South extending up to the Midwest, with reductions in area from HIST of 38%–45%. In addition to decreasing in spatial extent, distributions in future SON epochs are shifted towards the west into the southern Great Plains. Prior work has shown that reductions in ellipse area correspond to increased spatial concentration of tornado activity (Moore and McGuire 2019). In this context, the projected decrease in SON spatial extent suggests a potential increase in spatial concentration of SCS activity in the Deep South and southern Great Plains in future climates.

Monthly trends further illustrate spatiotemporal shifts of synthetic SCS counts in the ECONUS in future epochs. A clear, early-season trend emerges in all epochs, with February through April illustrating notable increases in SCS counts compared to HIST (Figure 10A,G). These gains in early-season SCS events are especially prominent in the southern Great Plains and the Southeast (Figure 10C,D,I,J). In the southern Great Plains, large increases in SCS events occur between February and May, and large decreases occur in June and July, except for MID8.5 (Figure 10C,I). In the northern Great Plains, SCS frequency increases in April through June but declines sharply during July and August (Figure 10B,H).

The Southeast has projected increases in SCS frequency in most months across all future epochs, with the largest gains during JJA, suggesting an enhanced year-round SCS risk for this particularly vulnerable region (Figure 10D,J). In the Midwest, projections suggest a steady increase in SCS counts from spring through summer, while the Northeast is expected to see increases in SCS events almost exclusively in JJA (Figure 10E,F,K,L). Generally, all future epochs show a persistent JJA SCS peak; however, the geographic pattern in SCS events is expected to shift eastward and northward from its historical extent (Brooks et al. 2003; Cintineo et al. 2012; Smith et al. 2012; Murillo et al. 2021).

Results confirm that the eastward trend in heightened SCS frequency documented in recent decades (Gensini and Brooks 2018; Moore 2025; Kiefer et al. 2025) is projected to persist, with increases across the Midwest, Southeast and Northeast and decreases in the southern and central Great Plains during JJA. These future trends are consistent with Lee (2012) and Hoogewind et al. (2017), who project increased tornado and SCS days in the Great Plains, Midwest and Southeast and reductions in the southern Great Plains. This projected eastward shift in the heightened SCS climatology places increasing SCS activity in regions with greater population and built environment density, potentially altering the probability of disaster occurrence and impacts (Ashley et al. 2014; Strader et al. 2024).

3.5 | High-Impact Days

Prior literature has been inconsistent in defining what constitutes an SCS or tornado outbreak or high-impact day (Ćwik

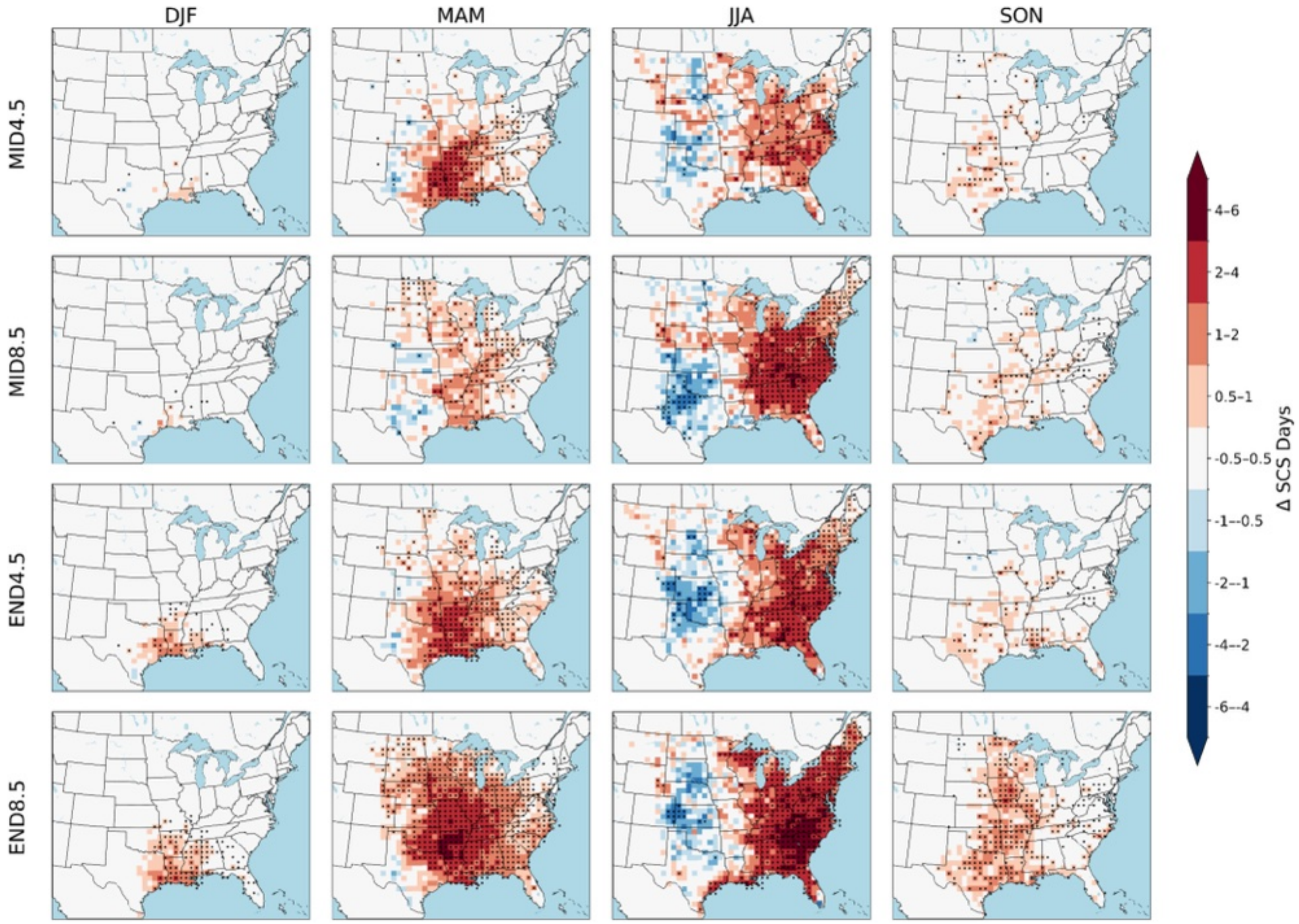

FIGURE 8 | Spatial deltas, showing differences in the number of SCS days between each epoch (rows) and the historical baseline for each season (columns). SCS days are the monthly means for each future epoch relative to HIST. Red shading indicates increases in SCS days, while blue shading indicates a decrease in SCS days. Stippling marks regions of statistical significance based on the Mann–Whitney *U*-test. [Colour figure can be viewed at wileyonlinelibrary.com]

et al. 2021). High-impact events and outbreaks have been characterised using fixed daily or fixed event counts (e.g., Galway 1977; Johns 1982; Tippett et al. 2016), cluster size (e.g., Galway 1977), weighted peril ranking (e.g., Doswell et al. 2006), regression-based thresholds (e.g., Verbout et al. 2006) and severity categories based on Fujita ratings (e.g., Schneider et al. 2004). Because criteria vary widely by study and with a predominant focus on tornadoes as opposed to all SCS perils, high-impact days are defined here as the upper tail of the synthetic daily SCS detection count distribution, analysed as the 90th percentile of domain-wide daily counts of threshold-exceeding synthetic proxy SCS detections along with their associated probabilities of exceedance (POEs). Daily SCS counts are calculated for convective days with at least one threshold-exceeding synthetic detection in the domain. This percentile-based framework avoids reliance on a single arbitrary outbreak definition and storm object identification and provides a direct assessment of how the most active SCS days evolve in future climates.

High-impact days—defined here as days exceeding the 90th percentile of the synthetic daily SCS detection count distribution—are 32%–82% more frequent across future epochs compared to HIST (Figure 11, Table 4). In HIST, the 90th percentile threshold corresponds to 452 synthetic SCS detections per day across the ECONUS (Table 4). By mid-century, the 90th percentile threshold increases to 544–554 detections per day. By the end of the century, thresholds are projected to rise to 566–660 detections per day, indicating an escalation in the upper tail of the synthetic SCS detection count distribution. The probability of exceeding the historical 90th percentile threshold rises from 10% in HIST to 18% in END8.5, representing a near doubling of the likelihood that historically rare, high-activity SCS days may become more frequent by the end of the century. The overall distribution shifts towards higher daily detection counts, implying that both typical and upper-tail SCS days are projected to become more common in the future. The largest increases occur in END8.5, underscoring the sensitivity of simulated SCS frequency to greenhouse gas emissions pathways.

3.6 | Environmental Ingredients

Fundamental ingredients that support the development and sustenance of SCS broadly support the observed and projected spatiotemporal changes in synthetic SCS activity. Among these ingredients, thermodynamic instability, CIN and vertical wind shear show robust and consistent shifts under future emissions scenarios, providing some physical context for the projected SCS

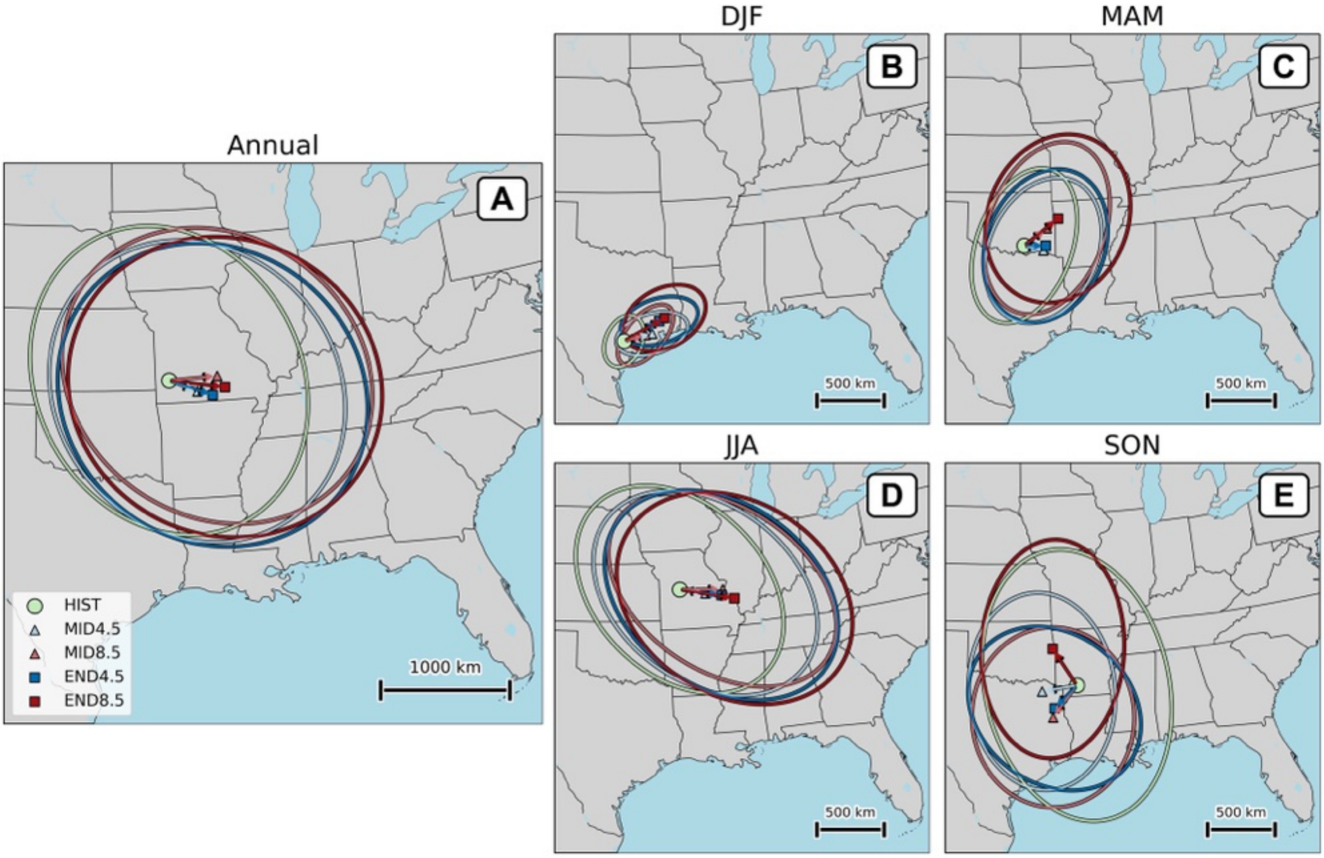

FIGURE 9 | Centroid of synthetic mean SCS days per year masked at ≥1 day/year; dispersion ellipses derived from the weighted spatial covariance of SCS days and the vector shift from the HIST centroid to each future epoch centroid for (A) annual, (B) winter (DJF), (C) spring (MAM), (D) summer (JJA) and (E) fall (SON). Colours for epochs are as in Figure 7, with a circle representing HIST, triangles representing mid-century and squares representing end-of-century epochs. [Colour figure can be viewed at wileyonlinelibrary.com]

changes described above. These results expand on prior work with WRF-BCC ingredients' output by providing seasonal climatologies of vertical wind shear and quantitative output for environmental variables (Figures S4–S6).

Instability, as measured via the most unstable CAPE (MUCAPE) from WRF-BCC, shows projected increases across all future epochs, with annual mean increases ranging from 17% to 56% relative to HIST (Table 5). These increases are consistent across all future scenarios and align with earlier work demonstrating large historical (Taszarek et al. 2021) and end-of-century CAPE increases over the CONUS (Trapp, Halvorson, and Diffenbaugh 2007; Paquin et al. 2014; Seeley and Romps 2015; Hoogewind et al. 2017; Haberlie et al. 2022; Ashley et al. 2023). Rising MUCAPE during this period is consistent with the Clausius-Clapeyron scaling of moisture with temperature, where saturation vapour pressure increases by ~6%–7% per degree Celsius warming, enhancing parcel buoyancy (Seeley and Romps 2015; Agard and Emanuel 2017; Wang and Moyer 2023). Additionally, projected changes in MUCAPE may result from increasingly steeper tropospheric lapse rates in the midlatitudes (Brogli et al. 2021). Seasonal patterns in projected MUCAPE mirror peril results (Figure S4) with DJF increases along the Gulf Coast and Southeast, springtime growth across the southern Great Plains spreading into the Midwest and Northeast and summer increases in the northern Great Plains and Great Lakes, with relative declines in the central Great Plains. These trends provide a thermodynamic context for and are coincident with the earlier seasonal onset of SCS frequency and its eastward and northward shift.

At the same time, projected environments become increasingly capped. Mean most unstable CIN (MUCIN) from WRF-BCC is projected to rise by 10%–35% across epochs in areas at relatively high risk for SCSs, with the largest increases in the Great Plains and during the warm season (Figure 12C, Figure S5). These findings are consistent with prior modelling (Hoogewind et al. 2017; Rasmussen et al. 2020; Chen et al. 2020; Haberlie et al. 2022; Ashley et al. 2023) and observed increases in capping in the climatological record (Taszarek et al. 2021; Andrews et al. 2024). Stronger capping complicates the notion that higher instability produces more SCSs. While stronger capping may limit convective initiation in some settings, it can also create ‘loaded gun’ environments where explosive, high-impact storms occur once inhibition is breached (Rasmussen et al. 2020), particularly in regions like the southern Great Plains where very high CAPE can coexist with strong CIN. This may help explain why explicit simulations in this analysis show both regions and seasons with declines in SCS days as well as regions and seasons with *more* frequent high-impact peril days, even as capping intensifies.

Changes in vertical wind shear are more modest, with small annual mean decreases of 2%–5% (Figure 12, Figure S6). However,

TABLE 3 | Centroid shift (difference between each future epoch centroid and HIST centroid, in km), ellipse area (computed from the eigendecomposition of a weighted spatial covariance matrix of synthetic severe convective storm [SCS] days, in km^2) and the area change (in %) of SCS days for the annual and seasonal means of each epoch.

Annual	Centroid shift (km)	Ellipse area (km^2)	Area change (%)
HIST	—	1.07×10^6	—
MID4.5	121.4	1.12×10^6	+4.5
MID8.5	194.2	1.15×10^6	+7.2
END4.5	184.8	1.18×10^6	+10.3
END8.5	226.6	1.19×10^6	+11.0
DJF			
HIST	—	5.17×10^4	—
MID4.5	165.1	7.68×10^4	+48.6
MID8.5	127.2	7.21×10^4	+39.4
END4.5	231.5	9.40×10^4	+81.9
END8.5	266.8	1.35×10^5	+161.0
MAM			
HIST	—	4.03×10^5	—
MID4.5	113.6	4.29×10^5	+6.5
MID8.5	165.5	5.43×10^5	+34.8
END4.5	122.8	4.88×10^5	+21.0
END8.5	250.0	6.31×10^5	+56.6
JJA			
HIST	—	1.07×10^6	—
MID4.5	149.8	1.14×10^6	+6.9
MID8.5	246.7	1.07×10^6	+0.9
END4.5	243.6	1.22×10^6	+14.5
END8.5	320.8	1.27×10^6	+19.1
SON			
HIST	—	1.32×10^6	—
MID4.5	203.3	7.55×10^5	−42.9
MID8.5	229.8	7.64×10^5	−42.3
END4.5	185.8	7.24×10^5	−45.3
END8.5	252.8	8.18×10^5	−38.2

seasonally and regionally, small shear changes are important for convective severity. Projected increases in deep-layer vertical wind shear (0–6 km) appear in DJF across the Southeast and in MAM across the central Plains and Midwest, coinciding with projected instability-driven increases in SCS frequency during these seasons. Conversely, SON exhibits widespread projected shear decreases, consistent with diminished peril frequency in late autumn. These patterns align with earlier findings that, while CAPE dominates future increases in severe potential, the seasonal overlap of shear with unstable environments continues to modulate SCS risk (Diffenbaugh et al. 2013; Hoogewind et al. 2017).

When these ingredients are considered in concert, findings emphasise the complexity of SCS environments in a warming climate. Rising CAPE, driven by higher moisture availability, provides greater storm potential, while stronger capping modulates when and where that potential is realised. Shear changes introduce regional and seasonal nuance, with localised increases during MAM and JJA enhancing SCS risk in spring, but widespread decreases during SON that act to reduce SCS risk in the autumn throughout the domain. The overlap of these factors provides environmental context for the projected eastward shift in—or broadening of the overall—ECONUS SCS climatology, consistent with the eastward change and earlier seasonal onset of SCS frequency projected in these simulations. Importantly, explicitly resolving perils permits capturing not only whether these favourable thermodynamic environments are present but also whether sufficient forcing is present to overcome inhibition and initiate storms—adding critical nuance for the potential realisation of SCSs beyond environmental proxies alone.

4 | Conclusion

This research provides one of the first convection-permitting assessments of the projected evolution of SCS activity across the ECONUS spanning both mid-century and end-century periods under multiple emission pathways. Importantly, this study extends beyond the end-of-century, high-emissions scenario focus and environmental-only perspectives common in the literature by demonstrating that measurable changes in SCS climatology emerge as early as mid-century and are evident across both intermediate and pessimistic warming trajectories. Overall findings point to a spatial reorganisation of SCS activity represented by an eastward shift and expansion of the areal extent of maximum SCS frequency into more densely populated regions; an earlier start and extension of the convective season; increased frequency of SCS events and days, including high-impact (upper-tail) activity days; greater availability of convectively favourable environments and a rise in nocturnal SCS events. These changes are accompanied by projected increases in instability and regionally varying changes in inhibition and deep-layer shear that provide physical context for the simulated SCS shifts. Taken together, results support the conclusion that ACC has the potential to reshape the spatiotemporal climatology of SCS activity across the ECONUS. These changes would have societal consequences, with projections suggesting that more individuals, homes and infrastructure could be at risk from SCS activity in the future. The explicit convection-permitting output generated from WRF-BCC permitted an exploration of the complex interplay of dynamic and thermodynamic factors, offering more important details to the broader changing SCS climatology story than that solely provided using an implicit or PGW explicit approach.

Collectively, these results suggest that the future ECONUS SCS landscape may become more active in parts of the Southeast, Midwest and Northeast, while portions of the Great Plains

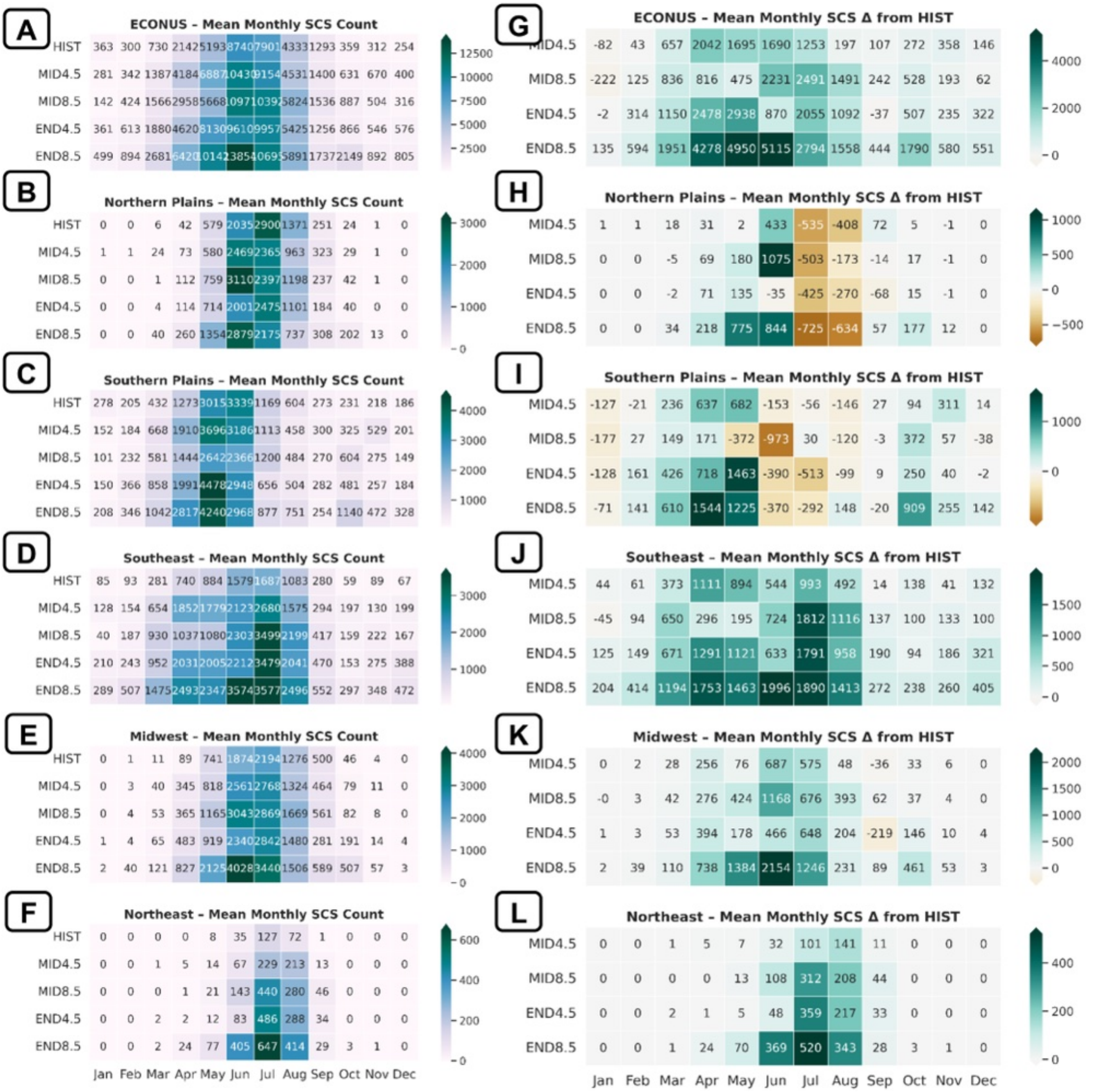

FIGURE 10 | Chiclet charts of synthetic mean monthly severe convective storm (SCS) counts for each epoch (A–F), with darker colours denoting higher counts. Panels (G–L) show mean monthly deltas, calculated as differences between each epoch and HIST, with green shading indicating increases relative to HIST and brown shading indicating decreases. Regions are defined by latitude and longitude bounds, which are illustrated in Figure S3. [Colour figure can be viewed at wileyonlinelibrary.com]

experience seasonal declines, particularly during summer. The projected eastward shift is notable because it places a greater share of SCS activity in regions with dense populations and built infrastructure, highlighting the importance of continued research into how changing storm climatology may intersect with evolving exposure and vulnerability. At the same time, these results should be interpreted within the limits of the proxy framework. The UVV + *Z* proxy is designed to represent broad SCS activity and does not directly identify realised hazard type, distinguish tornadoes from hail or wind or resolve conditional intensity distributions such as tornado occurrence by EF scale or wind events by measured severity. Accordingly, this study does not provide direct evidence for societal impacts of high-impact events (e.g., property loss and fatalities) but rather projected broad SCS and upper-tail SCS activity. Future work should evaluate individual hazards and spatial variations in proxy skill as well as societal impacts. Additionally, the proxy formulation may under-represent events occurring in marginal or nontraditional environments, such as high-shear, low-CAPE (HSLC); shallow convection and/or mesocyclones or cold-core systems (Davies 2006; Edwards et al. 2012; Sherburn and Parker 2014; Lyons et al. 2026). Expanding proxy definitions to better capture

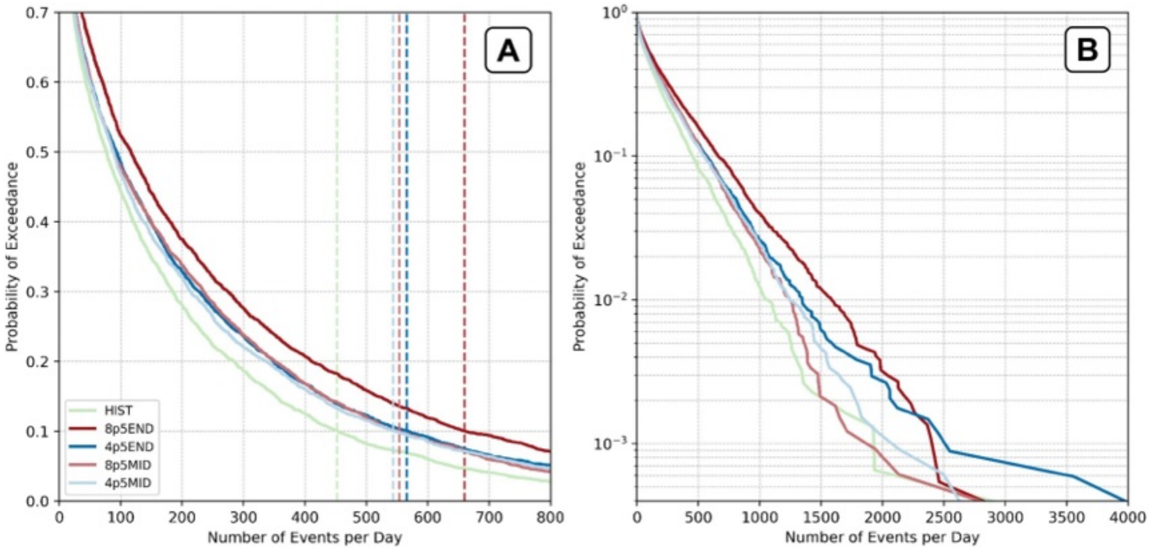

FIGURE 11 | Probability of exceedance (POE) of daily domain-wide counts of synthetic severe convective storm (SCS) detections for each epoch. (A) Results on a linear scale, with HIST in green, RCP4.5 in blue and RCP8.5 in red; MID epochs are shown in lighter shades and END epochs in darker shades. Dashed lines mark the 90th percentile for each epoch. (B) As in (A), but on a logarithmic scale to highlight behaviour in the extreme tail of the distribution. [Colour figure can be viewed at wileyonlinelibrary.com]

TABLE 4 | Mean, median (50th percentile), 90th, 95th and 99th percentiles of daily synthetic detection count distribution. Also shown are the POE at the HIST 90th percentile threshold and the per cent change relative to the HIST 90th percentile exceedance probability for each epoch.

Epoch	Mean	Median/50th Pct	90th Pct	95th Pct	99th Pct	POE at HIST 90 Pct	% Chg. vs. HIST 90 Pct
HIST	168	77	452	637	1039	—	—
MID4.5	197	88	544	772	1237	0.132	31.7
MID8.5	201	88	554	747	1239	0.141	41.0
END4.5	207	93	566	807	1344	0.139	38.8
END8.5	246	117	660	908	1579	0.182	82.0

TABLE 5 | Annual mean and median per cent differences of MUCAPE, MUCIN and 0–6 km wind shear for HIST, MID and END epochs.

	MUCAPE		MUCIN		0–6 km shear	
Epoch	Mean	Median	Mean	Median	Mean	Median
MID4.5	17.45%	41.85%	10.12%	14.81%	−1.81%	−3.07%
MID8.5	22.02%	35.64%	18.35%	31.50%	−1.83%	−3.52%
END4.5	24.73%	58.53%	13.61%	23.79%	−2.98%	−3.10%
END8.5	56.23%	171.25%	35.09%	54.50%	−5.23%	−7.84%

these environments represents an important avenue for future work, particularly given their potential for high societal impact.

Given the societal and economic importance of SCS peril forecasting and mitigation, ongoing research must continue to build on these initial efforts. As computing resources improve, future research using additional dynamically downscaled simulations in an ensemble approach, alongside additional GCM inputs, microphysics and PBL schemes over a longer climatological period will assist in quantifying uncertainty. Complementary implicit or ingredient-based studies will continue to improve our understanding of the ACC-induced mechanisms behind the changes projected to occur. The exploration of the roles of large-scale modes of climate interannual variability (e.g., ENSO, Gulf of Mexico surface temperature anomalies) will also be key to improving skilful subseasonal forecasts to decadal projections of SCSs. Additional work is needed to determine the local risks to the built environment and human vulnerability, as well as public policy and mitigation efforts for reducing the societal and economic impacts of SCSs, no matter their underlying

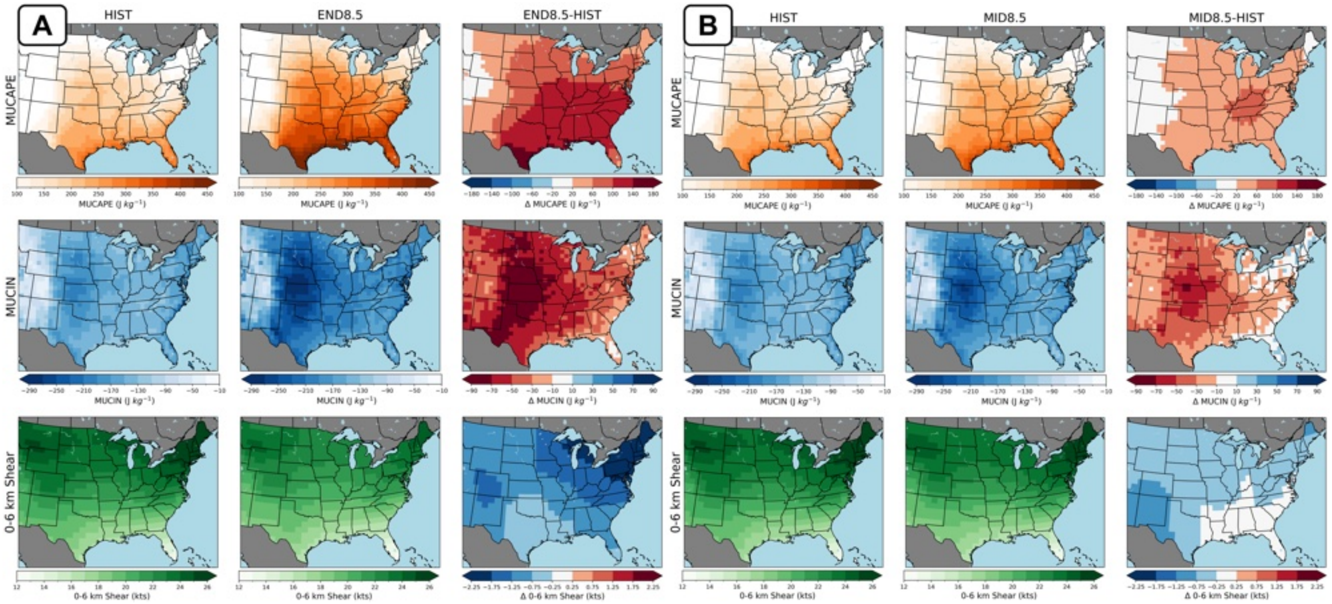

FIGURE 12 | (A) Spatial climatology of annual mean MUCAPE, MUCIN and 0–6 km wind shear for HIST, END8.5 and the difference between END8.5 and HIST. (B) As in (A), but for MID8.5. [Colour figure can be viewed at wileyonlinelibrary.com]

cause. This study provides one of the first explicit, convection-permitting assessments of how the broad SCS peril landscape in the ECONUS may change as we move through the 21st century by identifying the regions and seasons that are potentially at increased SCS risk, providing stakeholders with actionable information to generate more informed decisions to protect lives and advance economic prosperity in the United States.

Author Contributions

Caitlin M. Roufa: investigation, writing – original draft, methodology, conceptualization, validation, visualization, writing – review and editing, software, formal analysis, project administration, data curation. **Alex M. Haberlie:** writing – review and editing, supervision, resources. **Walker S. Ashley:** supervision, resources, conceptualization, funding acquisition, writing – review and editing, project administration. **Jeremy M. Corner:** validation, visualization, formal analysis, software, methodology, data curation, writing – review and editing, investigation. **Kelvin T. Hawthorne:** writing – review and editing, visualization, validation, investigation. **Landon K. Moeller:** validation, visualization, writing – review and editing, investigation. **Allison C. Michaelis:** writing – review and editing, resources, data curation. **Vittorio A. Gensini:** writing – review and editing, resources, data curation.

Acknowledgements

This research was supported by the National Science Foundation Awards 1637225 and 1800582 and the National Oceanic and Atmospheric Administration Award NA22OAR4690645. The authors acknowledge high-performance computing support from Cheyenne (https://doi.org/10.5065/D6RX99HX) provided by NCAR's Computational and Information Systems Laboratory, sponsored by the National Science Foundation. We also acknowledge and thank Dr. Michael Papka (ANL) for data storage and postprocessing assistance. This research used resources of the Argonne Leadership Computing Facility, a DOE Office of Science User Facility supported under Contract DE-AC02-06CH11357. Midcentury simulations were conducted using the Comet supercomputer, hosted by the San Diego Supercomputer Center at the University of California, San Diego. Compute time on Comet was made available by the Atmospheric River Program (Phases 2 and 3), which is supported by the California Department of Water Resources (awards 4600013361 and 4600014294, respectively) and the US Army Corps of Engineers Engineer Research and Development Center (award USACE W912HZ-15-2-0019).

Funding

This study was supported by the National Science Foundation (Awards 1637225 and 1800582), the National Oceanic and Atmospheric Administration (Award NA22OAR4690645), the Argonne Leadership Computing Facility (Contract DE-AC02-06CH11357), the California Department of Water Resources (Awards 4600013361 and 4600014294) and the U.S. Army Corps of Engineers Engineer Research and Development Center (Award W912HZ-15-2-0019).

Conflicts of Interest

The authors declare no conflicts of interest.

Data Availability Statement

In the spirit of reproducibility, if an email request is made to the authors, we will make available data and materials necessary to interested researchers for duplication and verification of results herein. WRF-BCC simulation output is available in netCDF format and stored on Argonne systems. Anyone interested in using the WRF-BCC output is encouraged to contact coauthor Gensini (vgensini@niu.edu) for information on how to access the data.

References

Agard, V., and K. Emanuel. 2017. "Clausius–Clapeyron Scaling of Peak CAPE in Continental Convective Storm Environments." *Journal of the Atmospheric Sciences* 74: 3043–3054. https://doi.org/10.1175/JAS-D-16-0352.1.

Allen, J. T., and M. K. Tippett. 2015. "The Characteristics of United States Hail Reports: 1955-2014." *E-Journal of Severe Storms Meteorology* 10: 1–31. https://doi.org/10.55599/ejssm.v10i3.60.

Andrews, M. S., V. A. Gensini, A. M. Haberlie, W. S. Ashley, A. C. Michaelis, and M. Taszarek. 2024. "Climatology of the Elevated Mixed

Layer Over the Contiguous United States and Northern Mexico Using ERA5: 1979–2021.” *Journal of Climate* 37: 1833–1851. https://doi.org/10.1175/JCLI-D-23-0517.1.

Antonio, B., and L. Aitchison. 2025. “How to Derive Skill From the Fractions Skill Score.” *Monthly Weather Review* 153: 1021–1033. https://doi.org/10.1175/MWR-D-24-0120.1.

AON. 2023. “Rising Losses From Severe Convection Storms Mostly Explained by Exposure Growth.” https://www.aon.com/en/insights/articles/rising-losses-from-severe-convection-storms-mostly-explained-by-exposure-growth?collection=e201f778-5b33-494e-9147-a3e899f05b09.

Ashley, W. S., A. M. Haberlie, and V. A. Gensini. 2023. “The Future of Supercells in the United States.” *Bulletin of the American Meteorological Society* 104: E1–E21. https://doi.org/10.1175/BAMS-D-22-0027.1.

Ashley, W. S., A. J. Krmenec, and R. Schwantes. 2008. “Vulnerability due to Nocturnal Tornadoes.” *Weather and Forecasting* 23: 795–807. https://doi.org/10.1175/2008WAF2222132.1.

Ashley, W. S., S. Strader, T. Rosencrants, and A. J. Krmenec. 2014. “Spatiotemporal Changes in Tornado Hazard Exposure: The Case of the Expanding Bull's-Eye Effect in Chicago, Illinois.” *Weather, Climate, and Society* 6: 175–193. https://doi.org/10.1175/WCAS-D-13-00047.1.

Black, A. W., and W. S. Ashley. 2010. “Nontornadic Convective Wind Fatalities in the United States.” *Natural Hazards* 54: 355–366. https://doi.org/10.1007/s11069-009-9472-2.

Brimelow, J. C., W. R. Burrows, and J. M. Hanesiak. 2017. “The Changing Hail Threat Over North America in Response to Anthropogenic Climate Change.” *Nature Climate Change* 7: 516–522. https://doi.org/10.1038/nclimate3321.

Brogli, R., S. Lund Sørland, N. Kröner, and C. Schär. 2021. “Future Summer Warming Pattern Under Climate Change Is Affected by Lapse-Rate Changes.” *Weather and Climate Dynamics* 2: 1093–1110. https://doi.org/10.5194/wcd-2-1093-2021.

Brooks, H. E. 2013. “Severe Thunderstorms and Climate Change.” *Atmospheric Research* 123: 129–138. https://doi.org/10.1016/j.atmosres.2012.04.002.

Brooks, H. E., C. A. Doswell, and M. P. Kay. 2003. “Climatological Estimates of Local Daily Tornado Probability for the United States.” *Weather and Forecasting* 18: 626–640.

Brown, M. C., C. J. Nowotarski, A. R. Dean, B. T. Smith, R. L. Thompson, and J. M. Peters. 2021. “The Early Evening Transition in Southeastern U.S. Tornado Environments.” *Weather and Forecasting* 36: 1431–1452. https://doi.org/10.1175/WAF-D-20-0191.1.

Bruyère, C. L., J. M. Done, G. J. Holland, and S. Fredrick. 2014. “Bias Corrections of Global Models for Regional Climate Simulations of High-Impact Weather.” *Climate Dynamics* 43: 1847–1856. https://doi.org/10.1007/s00382-013-2011-6.

Bundy, L. R., V. A. Gensini, and M. S. Russo. 2022. “Insured Corn Losses in the United States From Weather and Climate Perils.” *Journal of Applied Meteorology and Climatology* 61: 969–988. https://doi.org/10.1175/JAMC-D-21-0245.1.

Bunker, R. C., A. E. Cohen, J. A. Hart, A. E. Gerard, K. E. Klockow-McClain, and D. P. Nowicki. 2019. “Examination of the Predictability of Nocturnal Tornado Events in the Southeastern United States.” *Weather and Forecasting* 34: 467–479. https://doi.org/10.1175/WAF-D-18-0162.1.

Carley, J. R., B. R. J. Schwedler, M. E. Baldwin, et al. 2011. “A Proposed Model-Based Methodology for Feature-Specific Prediction for High-Impact Weather.” *Weather and Forecasting* 26: 243–249. https://doi.org/10.1175/WAF-D-10-05008.1.

Chen, J., A. Dai, Y. Zhang, and K. L. Rasmussen. 2020. “Changes in Convective Available Potential Energy and Convective Inhibition Under Global Warming.” *Journal of Climate* 33: 2025–2050. https://doi.org/10.1175/JCLI-D-19-0461.1.

Cintineo, J. L., T. M. Smith, V. Lakshmanan, H. E. Brooks, and K. L. Ortega. 2012. “An Objective High-Resolution Hail Climatology of the Contiguous United States.” *Weather and Forecasting* 27: 1235–1248. https://doi.org/10.1175/WAF-D-11-00151.1.

Clark, A. J., J. Gao, P. T. Marsh, et al. 2013. “Tornado Pathlength Forecasts From 2010 to 2011 Using Ensemble Updraft Helicity.” *Weather and Forecasting* 28: 387–407. https://doi.org/10.1175/WAF-D-12-00038.1.

Ćwik, P., R. A. McPherson, and H. E. Brooks. 2021. “What Is a Tornado Outbreak?: Perspectives Through Time.” *Bulletin of the American Meteorological Society* 102: E817–E835. https://doi.org/10.1175/BAMS-D-20-0076.1.

Davies, J. M. 2006. “Tornadoes With Cold Core 500-mb Lows.” *Weather and Forecasting* 21: 1051–1062. https://doi.org/10.1175/WAF967.1.

Dee, D. P., S. M. Uppala, A. J. Simmons, et al. 2011. “The ERA-Interim Reanalysis: Configuration and Performance of the Data Assimilation System.” *Quarterly Journal of the Royal Meteorological Society* 137: 553–597. https://doi.org/10.1002/qj.828.

Del Genio, A. D., M.-S. Yao, and J. Jonas. 2007. “Will Moist Convection Be Stronger in a Warmer Climate?” *Geophysical Research Letters* 34: L16703. https://doi.org/10.1029/2007GL030525.

Diffenbaugh, N. S., M. Scherer, and R. J. Trapp. 2013. “Robust Increases in Severe Thunderstorm Environments in Response to Greenhouse Forcing.” *Proceedings of the National Academy of Sciences of the United States of America* 110: 16361–16366. https://doi.org/10.1073/pnas.1307758110.

Doswell, C. A., R. Edwards, R. L. Thompson, J. A. Hart, and K. C. Crosbie. 2006. “A Simple and Flexible Method for Ranking Severe Weather Events.” *Weather and Forecasting* 21: 939–951. https://doi.org/10.1175/WAF959.1.

Ebert, E. E. 2008. “Fuzzy Verification of High-Resolution Gridded Forecasts: A Review and Proposed Framework.” *Meteorological Applications* 15: 51–64. https://doi.org/10.1002/met.25.

Ebert, E. E. 2009. “Neighborhood Verification: A Strategy for Rewarding Close Forecasts.” *Weather and Forecasting* 24: 1498–1510. https://doi.org/10.1175/2009WAF2222251.1.

Edwards, R., J. T. Allen, and G. W. Carbin. 2018. “Reliability and Climatological Impacts of Convective Wind Estimations.” *Journal of Applied Meteorology and Climatology* 57: 1825–1845. https://doi.org/10.1175/JAMC-D-17-0306.1.

Edwards, R., A. R. Dean, R. L. Thompson, and B. T. Smith. 2012. “Convective Modes for Significant Severe Thunderstorms in the Contiguous United States. Part III: Tropical Cyclone Tornadoes.” *Weather and Forecasting* 27: 1507–1519. https://doi.org/10.1175/WAF-D-11-00117.1.

Gallo, B. T., A. J. Clark, and S. R. Dembek. 2016. “Forecasting Tornadoes Using Convection-Permitting Ensembles.” *Weather and Forecasting* 31: 273–295. https://doi.org/10.1175/WAF-D-15-0134.1.

Galway, J. G. 1977. “Some Climatological Aspects of Tornado Outbreaks.” *Monthly Weather Review* 105: 477–484.

Gensini, V. A. 2021. “Severe Convective Storms in a Changing Climate.” In *Climate Change and Extreme Events*, edited by A. Fares, 39–56. Elsevier.

Gensini, V. A., W. S. Ashley, A. C. Michaelis, A. M. Haberlie, J. Goodin, and B. C. Wallace. 2024. “Hailstone Size Dichotomy in a Warming Climate.” *npj Climate and Atmospheric Science* 7: 185. https://doi.org/10.1038/s41612-024-00728-9.

Gensini, V. A., and H. E. Brooks. 2018. “Spatial Trends in United States Tornado Frequency.” *npj Climate and Atmospheric Science* 1: 38. https://doi.org/10.1038/s41612-018-0048-2.

Gensini, V. A., A. M. Haberlie, and W. S. Ashley. 2023. “Convection-Permitting Simulations of Historical and Possible Future Climate Over the Contiguous United States." *Climate Dynamics* 60: 109–126. https://doi.org/10.1007/s00382-022-06306-0.

Gensini, V. A., and T. L. Mote. 2014. "Estimations of Hazardous Convective Weather in the United States Using Dynamical Downscaling." *Journal of Climate* 27: 6581–6589. https://doi.org/10.1175/JCLI-D-13-00777.1.

Gensini, V. A., and T. L. Mote. 2015. "Downscaled Estimates of Late 21st Century Severe Weather From CCSM3." *Climatic Change* 129: 307–321. https://doi.org/10.1007/s10584-014-1320-z.

Gilleland, E., D. Ahijevych, B. G. Brown, B. Casati, and E. E. Ebert. 2009. "Intercomparison of Spatial Forecast Verification Methods." *Weather and Forecasting* 24: 1416–1430. https://doi.org/10.1175/2009WAF2222269.1.

Gilleland, E., D. A. Ahijevych, B. G. Brown, and E. E. Ebert. 2010. "Verifying Forecasts Spatially." *Bulletin of the American Meteorological Society* 91: 1365–1376. https://doi.org/10.1175/2010BAMS2819.1.

Glazer, R. H., J. A. Torres-Alavez, E. Coppola, et al. 2021. "Projected Changes to Severe Thunderstorm Environments as a Result of Twenty-First Century Warming From RegCM CORDEX-CORE Simulations." *Climate Dynamics* 57: 1595–1613. https://doi.org/10.1007/s00382-020-05439-4.

Haberlie, A. M., and W. S. Ashley. 2019. "Climatological Representation of Mesoscale Convective Systems in a Dynamically Downscaled Climate Simulation." *International Journal of Climatology* 39: 1144–1153. https://doi.org/10.1002/joc.5880.

Haberlie, A. M., W. S. Ashley, C. M. Battisto, and V. A. Gensini. 2022. "Thunderstorm Activity Under Intermediate and Extreme Climate Change Scenarios." *Geophysical Research Letters* 49: e2022GL098779. https://doi.org/10.1029/2022GL098779.

Hoogewind, K. A., M. E. Baldwin, and R. J. Trapp. 2017. "The Impact of Climate Change on Hazardous Convective Weather in the United States: Insight From High-Resolution Dynamical Downscaling." *Journal of Climate* 30: 10081–10100. https://doi.org/10.1175/JCLI-D-16-0885.1.

IPCC. 2014. *Climate Change 2014: AR5 Synthesis Report*. IPCC.

Johns, R. H. 1982. "A Synoptic Climatology of Northwest Flow Severe Weather Outbreaks. Part I: Nature and Significance." *Monthly Weather Review* 110: 1653–1663.

Kain, J. S., S. J. Weiss, D. R. Bright, et al. 2008. "Some Practical Considerations Regarding Horizontal Resolution in the First Generation of Operational Convection-Allowing NWP." *Weather and Forecasting* 23: 931–952. https://doi.org/10.1175/WAF2007106.1.

Kaminski, K., W. S. Ashley, A. M. Haberlie, and V. A. Gensini. 2024. "Future Derecho Potential in the United States." *Journal of Climate* 38: 3–26. https://doi.org/10.1175/JCLI-D-23-0633.1.

Kiefer, L., D. Chavas, M. Gore, and D. Dawson. 2025. "The Climatological Relationship Between United States Tornadoes and Extratropical Cyclones." Preprint, arXiv, July 22. https://doi.org/10.48550/arXiv.2507.16975.

Lee, C. C. 2012. "Utilizing Synoptic Climatological Methods to Assess the Impacts of Climate Change on Future Tornado-Favorable Environments." *Natural Hazards* 62: 325–343. https://doi.org/10.1007/s11069-011-9998-y.

Lefever, D. W. 1926. "Measuring Geographic Concentration by Means of the Standard Deviational Ellipse." *American Journal of Sociology* 32: 88–94. https://doi.org/10.1086/214027.

Lepore, C., R. Abernathey, N. Henderson, J. T. Allen, and M. K. Tippett. 2021. "Future Global Convective Environments in CMIP6 Models." *Earth's Future* 9: e2021EF002277. https://doi.org/10.1029/2021EF002277.

Liu, C., K. Ikeda, R. Rasmussen, et al. 2017. "Continental-Scale Convection-Permitting Modeling of the Current and Future Climate of North America." *Climate Dynamics* 49: 71–95. https://doi.org/10.1007/s00382-016-3327-9.

Lyons, A. D., R. L. Thompson, B. T. Smith, H. G. Weinman, and A. R. Dean. 2026. "Convective Mode Classification and Distribution of Contiguous U.S. Tornado Events From 2003 to 2023." *Weather and Forecasting* 41: 617–635. https://doi.org/10.1175/WAF-D-25-0034.1.

Mittermaier, M. P. 2021. "A "Meta" Analysis of the Fractions Skill Score: The Limiting Case and Implications for Aggregation." *Monthly Weather Review* 149: 3491–3504. https://doi.org/10.1175/MWR-D-18-0106.1.

Moore, T. W. 2025. "Isolating Tornado Trends: A Physically Informed Time Series Decomposition of the Great Plains and Southeast Tornado Records." Preprint, ResearchSquare, August 18. https://doi.org/10.21203/rs.3.rs-7214699/v1.

Moore, T. W., and M. P. McGuire. 2019. "Using the Standard Deviational Ellipse to Document Changes to the Spatial Dispersion of Seasonal Tornado Activity in the United States." *npj Climate and Atmospheric Science* 2: 21. https://doi.org/10.1038/s41612-019-0078-4.

Moss, R. H., J. A. Edmonds, K. A. Hibbard, et al. 2010. "The Next Generation of Scenarios for Climate Change Research and Assessment." *Nature* 463: 747–756. https://doi.org/10.1038/nature08823.

Murillo, E. M., C. R. Homeyer, and J. T. Allen. 2021. "A 23-Year Severe Hail Climatology Using GridRad MESH Observations." *Monthly Weather Review* 149: 945–958. https://doi.org/10.1175/MWR-D-20-0178.1.

Paquin, D., R. de Elía, and A. Frigon. 2014. "Change in North American Atmospheric Conditions Associated With Deep Convection and Severe Weather Using CRCM4 Climate Projections." *Atmosphere-Ocean* 52: 175–190. https://doi.org/10.1080/07055900.2013.877868.

Prein, A. F. 2023. "Thunderstorm Straight Line Winds Intensify With Climate Change." *Nature Climate Change* 13: 1353–1359. https://doi.org/10.1038/s41558-023-01852-9.

Pulkkinen, S., D. Nerini, A. A. Pérez Hortal, et al. 2019. "Pysteps: An Open-Source Python Library for Probabilistic Precipitation Nowcasting (v1.0)." *Geoscientific Model Development* 12: 4185–4219. https://doi.org/10.5194/gmd-12-4185-2019.

Rasmussen, K. L., A. F. Prein, R. M. Rasmussen, K. Ikeda, and C. Liu. 2020. "Changes in the Convective Population and Thermodynamic Environments in Convection-Permitting Regional Climate Simulations Over the United States." *Climate Dynamics* 55: 383–408. https://doi.org/10.1007/s00382-017-4000-7.

Rasmussen, R. M., F. Chen, C. H. Liu, et al. 2023. "CONUS404: The NCAR–USGS 4-km Long-Term Regional Hydroclimate Reanalysis Over the CONUS." *Bulletin of the American Meteorological Society* 104: E1382–E1408. https://doi.org/10.1175/BAMS-D-21-0326.1.

Raupach, T. H., O. Martius, J. T. Allen, et al. 2021. "The Effects of Climate Change on Hailstorms." *Nature Reviews Earth & Environment* 2: 213–226. https://doi.org/10.1038/s43017-020-00133-9.

Roberts, N. M., and H. W. Lean. 2008. "Scale-Selective Verification of Rainfall Accumulations From High-Resolution Forecasts of Convective Events." *Monthly Weather Review* 136: 78–97. https://doi.org/10.1175/2007MWR2123.1.

Robinson, E. D., R. J. Trapp, and M. E. Baldwin. 2013. "The Geospatial and Temporal Distributions of Severe Thunderstorms From High-Resolution Dynamical Downscaling." *Journal of Applied Meteorology and Climatology* 52: 2147–2161. https://doi.org/10.1175/JAMC-D-12-0131.1.

Schneider, R. S., H. E. Brooks, and J. T. Schaefer. 2004. "Tornado Outbreak Days: An Updated and Expanded Climatology (1875–2003)." https://ams.confex.com/ams/11aram22sls/techprogram/paper_82031.htm.

Seeley, J. T., and D. M. Romps. 2015. "The Effect of Global Warming on Severe Thunderstorms in the United States." *Journal of Climate* 28: 2443–2458. https://doi.org/10.1175/JCLI-D-14-00382.1.

Sherburn, K. D., and M. D. Parker. 2014. "Climatology and Ingredients of Significant Severe Convection in High-Shear, Low-CAPE Environments." *Weather and Forecasting* 29: 854–877. https://doi.org/10.1175/WAF-D-13-00041.1.

Skamarock, A. W., J. B. Klemp, J. Dudhia, et al. 2019. *A Description of the Advanced Research WRF Model Version 4.1*. National Science Foundation.

Skok, G. 2015. "Analysis of Fraction Skill Score Properties for a Displaced Rainband in a Rectangular Domain." *Meteorological Applications* 22: 477–484. https://doi.org/10.1002/met.1478.

Skok, G., and N. Roberts. 2016. "Analysis of Fractions Skill Score Properties for Random Precipitation Fields and ECMWF Forecasts." *Quarterly Journal of the Royal Meteorological Society* 142: 2599–2610. https://doi.org/10.1002/qj.2849.

Skok, G., and N. Roberts. 2018. "Estimating the Displacement in Precipitation Forecasts Using the Fractions Skill Score." *Quarterly Journal of the Royal Meteorological Society* 144: 414–425. https://doi.org/10.1002/qj.3212.

Smith, A. B. 2020. "U.S. Billion-Dollar Weather and Climate Disasters, 1980–Present (NCEI Accession 0209268)." https://www.ncei.noaa.gov/access/metadata/landing-page/bin/iso?id=gov.noaa.nodc:0209268.

Smith, B. T., R. L. Thompson, J. S. Grams, C. Broyles, and H. E. Brooks. 2012. "Convective Modes for Significant Severe Thunderstorms in the Contiguous United States. Part I: Storm Classification and Climatology." *Weather and Forecasting* 27: 1114–1135. https://doi.org/10.1175/WAF-D-11-00115.1.

Smith, P. L. 1999. "Effects of Imperfect Storm Reporting on the Verification of Weather Warnings." *Bulletin of the American Meteorological Society* 80: 1099–1106. https://doi.org/10.1175/1520-0477(1999)080%253C1099:EOISRO%253E2.0.CO;2.

Sobash, R., D. Bright, A. Dean, et al. 2008. "Severe Storm Forecast Guidance Based on Explicit Identification of Convective Phenomena in WRF-Model Forecasts." https://www.researchgate.net/profile/David-Bright-9/publication/228845468_Severe_storm_forecast_guidance_based_on_explicit_identification_of_convective_phenomena_in_WRF-model_forecasts/links/0c960527296222f08a000000/Severe-storm-forecast-guidance-based-on-explicit-identification-of-convective-phenomena-in-WRF-model-forecasts.pdf.

Sobash, R. A., and J. S. Kain. 2017. "Seasonal Variations in Severe Weather Forecast Skill in an Experimental Convection-Allowing Model." *Weather and Forecasting* 32: 1885–1902. https://doi.org/10.1175/WAF-D-17-0043.1.

Sobash, R. A., J. S. Kain, D. R. Bright, A. R. Dean, M. C. Coniglio, and S. J. Weiss. 2011. "Probabilistic Forecast Guidance for Severe Thunderstorms Based on the Identification of Extreme Phenomena in Convection-Allowing Model Forecasts." *Weather and Forecasting* 26: 714–728. https://doi.org/10.1175/WAF-D-10-05046.1.

Sobash, R. A., C. S. Schwartz, G. S. Romine, K. R. Fossell, and M. L. Weisman. 2016. "Severe Weather Prediction Using Storm Surrogates From an Ensemble Forecasting System." *Weather and Forecasting* 31: 255–271. https://doi.org/10.1175/WAF-D-15-0138.1.

SPC. 2024. "Severe Weather Database." https://www.spc.noaa.gov/wcm/.

Strader, S. M., W. S. Ashley, A. M. Haberlie, and K. Kaminski. 2022. "Revisiting U.S. Nocturnal Tornado Vulnerability and Its Influence on Tornado Impacts." *Weather, Climate, and Society* 14: 1147–1163. https://doi.org/10.1175/WCAS-D-22-0020.1.

Strader, S. M., W. S. Ashley, T. J. Pingel, and A. J. Krmenec. 2017. "Projected 21st Century Changes in Tornado Exposure, Risk, and Disaster Potential." *Climatic Change* 141: 301–313. https://doi.org/10.1007/s10584-017-1905-4.

Strader, S. M., V. A. Gensini, W. S. Ashley, and A. N. Wagner. 2024. "Changes in Tornado Risk and Societal Vulnerability Leading to Greater Tornado Impact Potential." *npj Natural Hazards* 1: 20. https://doi.org/10.1038/s44304-024-00019-6.

Taszarek, M., J. T. Allen, H. E. Brooks, N. Pilguj, and B. Czernecki. 2021. "Differing Trends in United States and European Severe Thunderstorm Environments in a Warming Climate." *Bulletin of the American Meteorological Society* 102: E296–E322. https://doi.org/10.1175/BAMS-D-20-0004.1.

Tippett, M. K., J. T. Allen, V. A. Gensini, and H. E. Brooks. 2015. "Climate and Hazardous Convective Weather." *Current Climate Change Reports* 1: 60–73. https://doi.org/10.1007/s40641-015-0006-6.

Tippett, M. K., C. Lepore, and J. E. Cohen. 2016. "More Tornadoes in the Most Extreme U.S. Tornado Outbreaks." *Science* 354: 1419–1423. https://doi.org/10.1126/science.aah7393.

Tirone, E., S. Pal, W. A. Gallus, et al. 2024. "A Machine Learning Approach to Improve the Usability of Severe Thunderstorm Wind Reports." *Bulletin of the American Meteorological Society* 105: E623–E638. https://doi.org/10.1175/BAMS-D-22-0268.1.

Trapp, R. J., N. S. Diffenbaugh, H. E. Brooks, M. E. Baldwin, E. D. Robinson, and J. S. Pal. 2007. "Changes in Severe Thunderstorm Environment Frequency During the 21st Century Caused by Anthropogenically Enhanced Global Radiative Forcing." *Proceedings of the National Academy of Sciences of the United States of America* 104: 19719–19723. https://doi.org/10.1073/pnas.0705494104.

Trapp, R. J., N. S. Diffenbaugh, and A. Gluhovsky. 2009. "Transient Response of Severe Thunderstorm Forcing to Elevated Greenhouse Gas Concentrations." *Geophysical Research Letters* 36. https://doi.org/10.1029/2008GL036203.

Trapp, R. J., B. A. Halvorson, and N. S. Diffenbaugh. 2007. "Telescoping, Multimodel Approaches to Evaluate Extreme Convective Weather Under Future Climates." *Journal of Geophysical Research: Atmospheres* 112: D20109. https://doi.org/10.1029/2006JD008345.

Trapp, R. J., and K. A. Hoogewind. 2016. "The Realization of Extreme Tornadic Storm Events Under Future Anthropogenic Climate Change." *Journal of Climate* 29: 5251–5265. https://doi.org/10.1175/JCLI-D-15-0623.1.

Trapp, R. J., K. A. Hoogewind, and S. Lasher-Trapp. 2019. "Future Changes in Hail Occurrence in the United States Determined Through Convection-Permitting Dynamical Downscaling." *Journal of Climate* 32: 5493–5509. https://doi.org/10.1175/JCLI-D-18-0740.1.

Trapp, R. J., E. D. Robinson, M. E. Baldwin, N. S. Diffenbaugh, and B. R. J. Schwedler. 2011. "Regional Climate of Hazardous Convective Weather Through High-Resolution Dynamical Downscaling." *Climate Dynamics* 37: 677–688. https://doi.org/10.1007/s00382-010-0826-y.

Trapp, R. J., D. M. Wheatley, N. T. Atkins, R. W. Przybylinski, and R. Wolf. 2006. "Buyer Beware: Some Words of Caution on the Use of Severe Wind Reports in Post Event Assessment and Research." *Weather and Forecasting* 21: 408–415. https://doi.org/10.1175/WAF925.1.

Van Klooster, S. L., and P. J. Roebber. 2009. "Surface-Based Convective Potential in the Contiguous United States in a Business-as-Usual Future Climate." *Journal of Climate* 22: 3317–3330. https://doi.org/10.1175/2009JCLI2697.1.

Verbout, S. M., H. E. Brooks, L. M. Leslie, and D. M. Schultz. 2006. "Evolution of the U.S. Tornado Database: 1954–2003." *Weather and Forecasting* 21: 86–93. https://doi.org/10.1175/WAF910.1.

Wang, B., W. Shi, and Z. Miao. 2015. "Confidence Analysis of Standard Deviational Ellipse and Its Extension Into Higher Dimensional Euclidean Space." *PLoS One* 10: e0118537. https://doi.org/10.1371/journal.pone.0118537.

Wang, S., R. J. Trapp, J. Allen, D. Gopalakrishnan, and E. Robinson. 2026. “Future Climate Projections of Hazardous Convective Weather Using an Ensemble of Environment-Informed, Convection-Permitting Dynamical Downscaling Simulations.” *Journal of Geophysical Research: Atmospheres* 131: e2025JD045354. https://doi.org/10.1029/2025JD045354.

Wang, Z., and E. J. Moyer. 2023. “Robust Relationship Between Midlatitudes CAPE and Moist Static Energy Surplus in Present and Future Simulations.” *Geophysical Research Letters* 50: e2023GL104163. https://doi.org/10.1029/2023GL104163.

Weiss, S. 2002. “An Examination of Severe Thunderstorm Wind Report Climatology: 1970–1999.” https://ams.confex.com/ams/SLS_WAF_NWP/techprogram/paper_47494.htm.

Wilks, D. S. 2019. *Statistical Methods in the Atmospheric Sciences*. Academic Press.

Supporting Information

Additional supporting information can be found online in the Supporting Information section. **Figure S1:** Spatial climatology of HIST exceedance days vs. SPC reports. **Figure S2:** Per cent change in SCS days. **Figure S3:** Regional spatial domains. **Figure S4:** Mean seasonal deltas of MUCAPE. **Figure S5:** Mean seasonal deltas of MUCIN. **Figure S6:** Mean seasonal deltas of deep-layer vertical wind shear.